Fatigue strength of solder joint in electronic assemblies exposed to combined temperature and vibration cyclic loading

Ključar, Luka

UNIVERSITY OF ZAGREB
FACULTY OF MECHANICAL ENGINEERING AND NAVAL ARCHITECTURE

MASTER'S THESIS

Luka Ključar

Zagreb, 2012.

UNIVERSITY OF ZAGREB
FACULTY OF MECHANICAL ENGINEERING AND NAVAL ARCHITECTURE

MASTER'S THESIS

Promoters:

Prof. dr. sc. Željko Božić
Prof. dr. sc. Ingrid De Wolf

Student:

Luka Ključar

Zagreb, 2012.

STATEMENT

I hereby declare that this thesis is entirely the result of my own work except where otherwise indicated. I have fully cited all used sources and I have only used the ones given in the list of references.

Luka Ključar

ACKNOWLEDGMENT

I would like to express my sincere gratitude to my Professor Željko Božić from Faculty of Mechanical Engineering and Naval Architecture for his guidance during the writing of my thesis. I would also like to extend that gratitude to Professor Ingrid De Wolf from imec for her help and encouragement during my internship in imec.

I also want express my sincere gratitude to my daily adviser at imec, Dr. Bart Vandevelde for his continuous help and support during my internship in imec throughout this work.

ABSTRACT

In this thesis an analysis of a simple PCB (Printed Circuit Board) under combined thermal and vibration loading has been conducted in order to estimate the fatigue life of the solder joints. This includes a FEM (Finite Element Method) dynamic and thermal analysis of solder joints. The goal was to develop a feasible FEM based methodology for combined thermal and vibration loading.

In order to increase the understanding the problem of the fatigue of solder joints, a number of theoretical fundamentals are given, which include an introduction to vibration fundamentals, which include basics of vibration of plates, time independent inelastic material behavior is described and an overview of LCF (Low Cycle Fatigue) and HCF (High Cycle Fatigue) is also given.

SAŽETAK

U ovom radu je izvršena analiza jednostavnog PCB-a (Printed Circuit Board) pod toplinskim i vibracijskim opterećenjem kako bi se odredio životni vijek lemljenih spojeva. Analiza uključuje toplinsku i dinamičku analizu metodom konačnih elemenata (MKE).

Kako bi se bolje razumio problem zamora lemljenih spojeva, dan je uvod u teorijske osnove vibracija, što uključuje vibracije ploča, uvod u vremenski neovsino neelastično ponašanje materijala, te je dan pregled LCF-a (Low Cycle Fatigue) i HCF-a (High Cycle Fatigue).

PROŠIRENI SAŽETAK

Elektronički sustavi u zrakoplovstvu predastavljaju jedan od ključnih sustava današnjih zrakoplovnih konstrukcija. Odgovorni su za povezivanje, ispravno funkcioniranje i nadziranje svih ostalih sustava zrakoplova. Stoga je izuzetno važno osigurati maksimalnu pouzdanost tih sustava. Za razliku od elektroničkih sustava u većini industrijskih pogona, kućanstava i ostalnim prometnim sredstvima, elektronička oprema u zrakoplovstvu podložna je cijelom nizu opterećenja, od toplinskih, vibracijskih, raznih tipova zračenja, itd. Njaveći uzrok kvarova i otkaza takve opreme predstavljaju upravo toplinska i vibracijska opterećenja. Kritični dijelovi opreme, oni koji će prvi otkazati, jesu lemljeni spojevi. Dok se u prošlosti radila analiza lemljenih spojeva pod samo toplinskim ili samo vibracijskim opterećenjem, ne postoji dovoljno razrađena FEM metodologija za analizu lemljenih spojeva pod istovremenim toplinskim i vibracijskim opterećenjem.

Stoga je cilj ovog rada bio razvijanje FEM metodologije za analizu lemljenih spojeva pod istovremenim toplinskim i vibracijskim opterećenjem. To uključuje modalnu analizu za dobivanje osnovnih parametara dinamičkog ponašanja PCB (vlastite frekvencije i modove vibriranja), analizu sustava pod toplinskim opterećenjem, kako bi se odredile plastične deformacije uslijed čistog toplinskog opterećenja, te analiza sustava opterećenog istovremenim toplinskim i vibracijskim opterećenjem.

Razvijena metoda je pokazala određene obećavajuće rezultate, te je dobra podloga za daljnje unaprjeđivanje kako bi se što točnije mogla izvršiti analiza lemljenih spojeva pod istovremenim toplinskim i vibracijskim opterećenjem.

Table of Contents

List of Figures

List of tables

List of symbols

E	Young's modulus
ν	Poisson's ratio
h	plate thickness
f	forcing frequency
f_n	eigenfrequency
A	amplification
Q	transmissibility
a	acceleration
g	gravitational acceleration
N_f	number of cycles to failure
D	damage
TTF	time to failure
$\Delta\varepsilon_{pl}$	total plastic strain in one cycle

1 Introduction

Today, electronics and electrical systems are a vital part of virtually every aircraft. On modern commercial airliners and military aircraft they control every essential component and its function, and the aircraft as a whole. These usually include engine control systems, flight control systems, fuel systems, pneumatic and hydraulic systems, environmental control systems, other advanced and emergency systems. First major breakthrough came after the WWII and the introduction of transistors. In the beginning, electrical systems served as engine control units, but the usage of electronics spread to every other system, flight controls included.

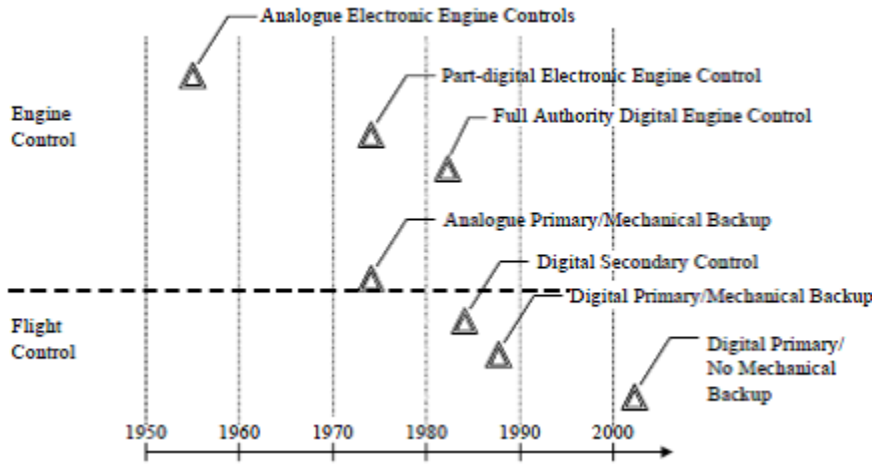

Figure 1. Major electronics development in aviation (1)

Also, the electrical systems are becoming more complex, more integrated and are located in almost every corner of the aircraft. While this has benefits, there are also several drawbacks to such systems. More advanced systems will provide better monitoring and supervision of the aircraft during mission operations. They also act as safety systems, preventing possible hazardous situations. They also give better feedback to the pilot. However, as mentioned, these systems need to be extremely reliable as they control every part of the plane and, in some cases, have greater control over the aircraft than pilot himself. It is therefore necessary to minimize any chance of possible failures of the electrical and electronic systems of the aircraft, as these kinds of failures can have catastrophic consequences.

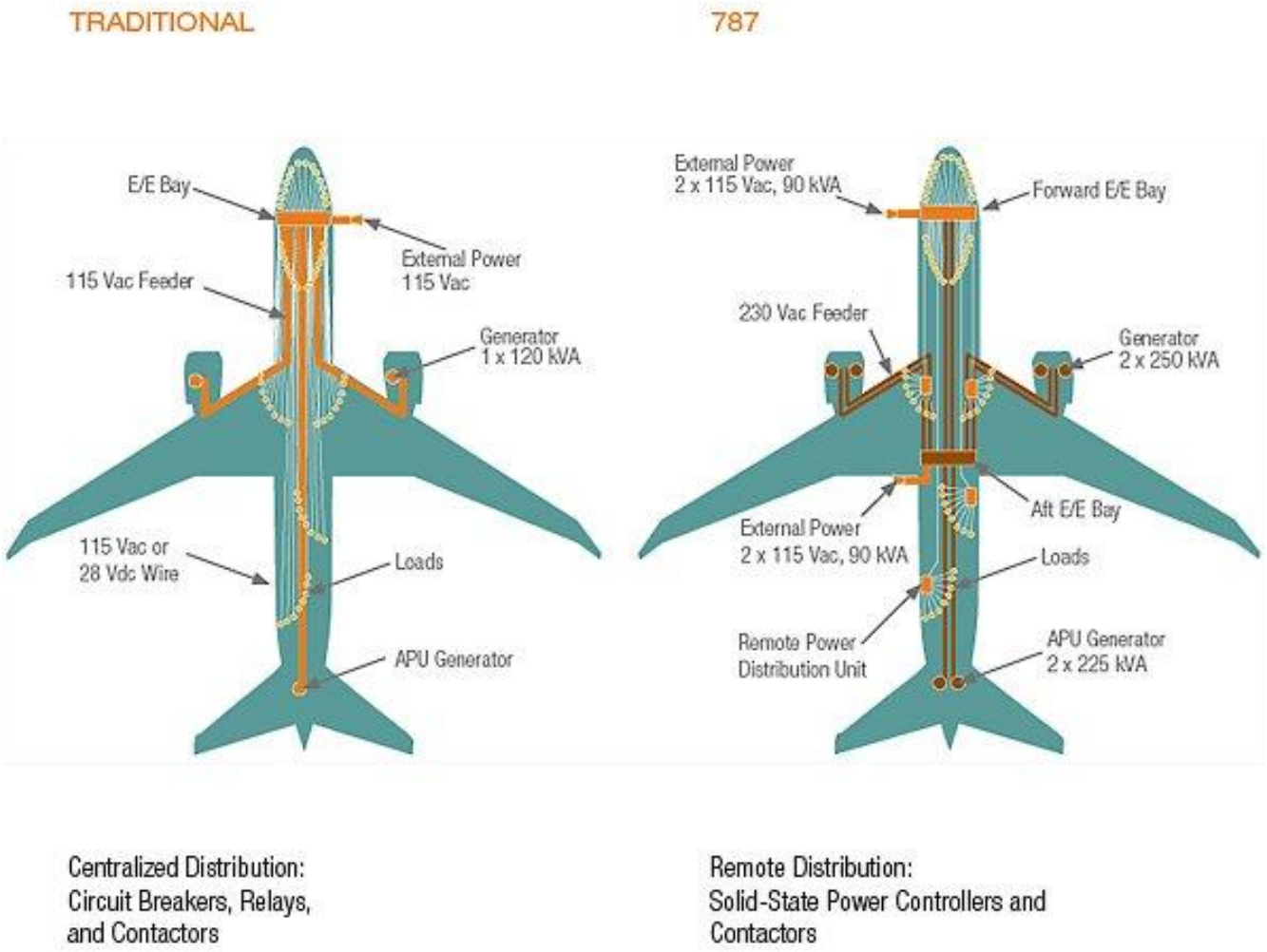

Figure 2. Comparison of traditional and Boeing 787 Electrical system distribution

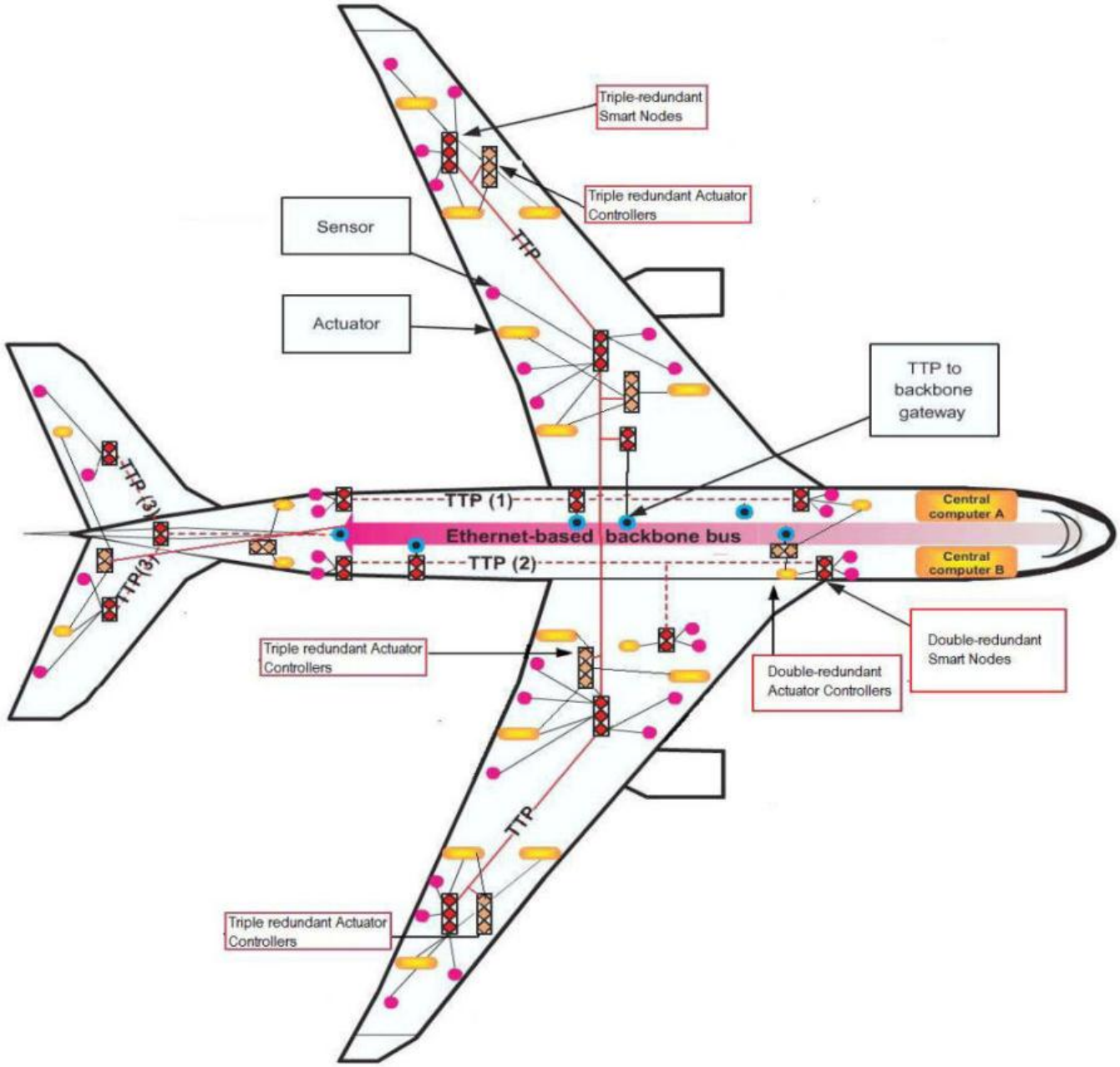

Figure 3. Redundant actuator controllers for a Time-triggered Protocol (TTP)-based integrated modular avionics subsystems

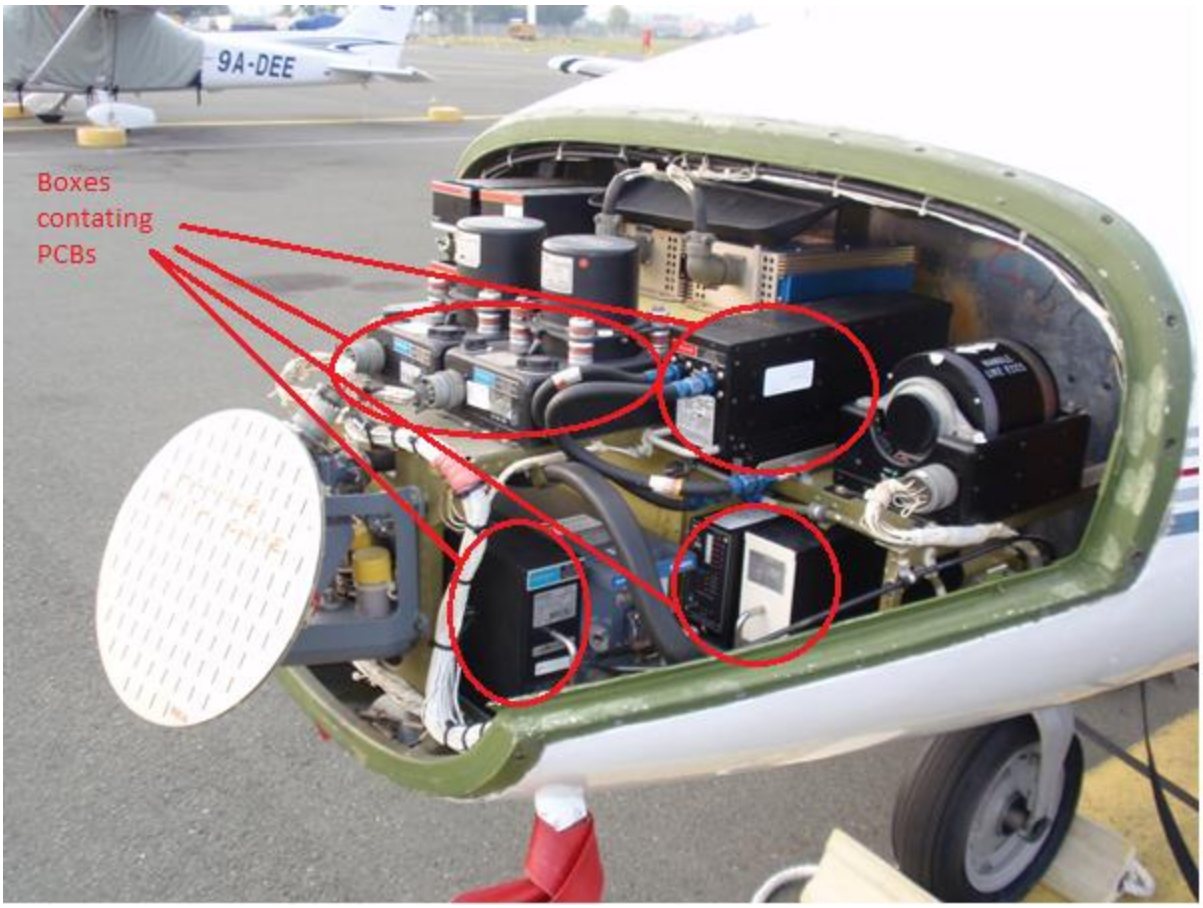

Figure 4. Cessna Citation radar and other avionics

Figure 5. AN/ASN-128B/C DOPPLER NAVIGATION SET BAE Systems

Also, unlike typical electronic products, electronic assemblies in aircraft are subjected to extreme environmental conditions. These are extremely high and low temperature, vibrations (shock), humidity, radiation, etc. All of these influence the reliability of electronic systems in the aircraft. However, the most significant causes of failures are extreme temperature and vibration conditions. Extreme temperature gradients are mainly caused by altitude changes and other environmental factors (such as geographical location of airports, etc).

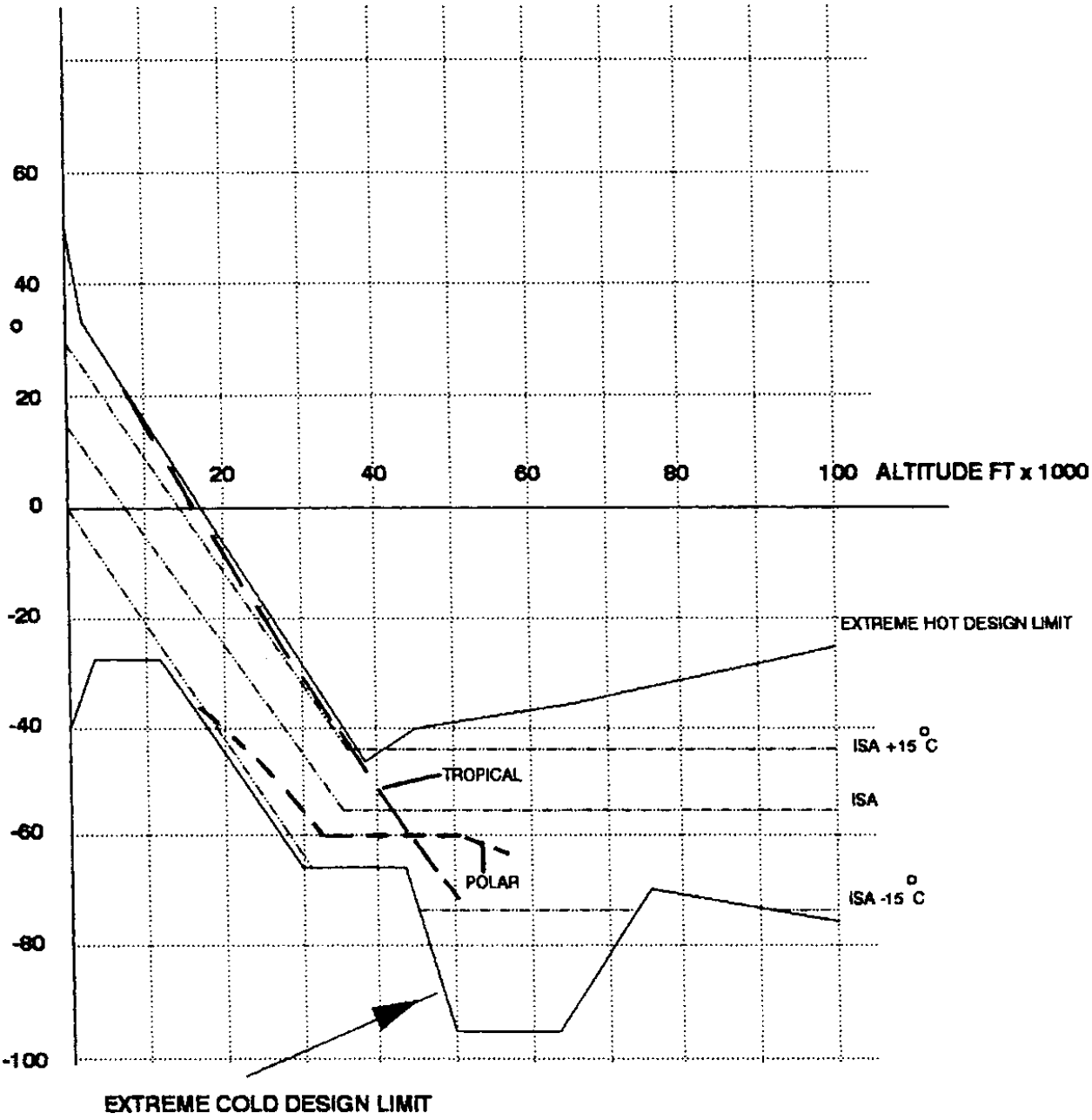

Figure 6. Ambient temperature versus altitude (1)

For less extreme environments (in case of local flights) the ambient temperature may vary from -10 to +30 degrees Celsius (2). The usual temperature span for avionics is from -40 to +90 degrees Celsius (1). Here, temperature cycling conditions (min and max temperatures) were selected based on JEDEC temperature cycling standard (JESD22-A104-B). The JEDEC Solid State Technology Association, formerly known as the Joint Electron Devices Engineering Council (JEDEC), is an independent semiconductor engineering trade organization and standardization body. The purpose of JEDEC is to develop standards for semiconductor industry. It has over 300 members, including Aeroflex, BAE Systems, U.S. Army, Mitsubishi, etc. Other

standard which is commonly used in aerospace industry is United States defense standard, usually called military standard or MIL-STD.

As mentioned today's aircraft systems are highly integrated. An example would be power generation system, environmental control system and fuel system.

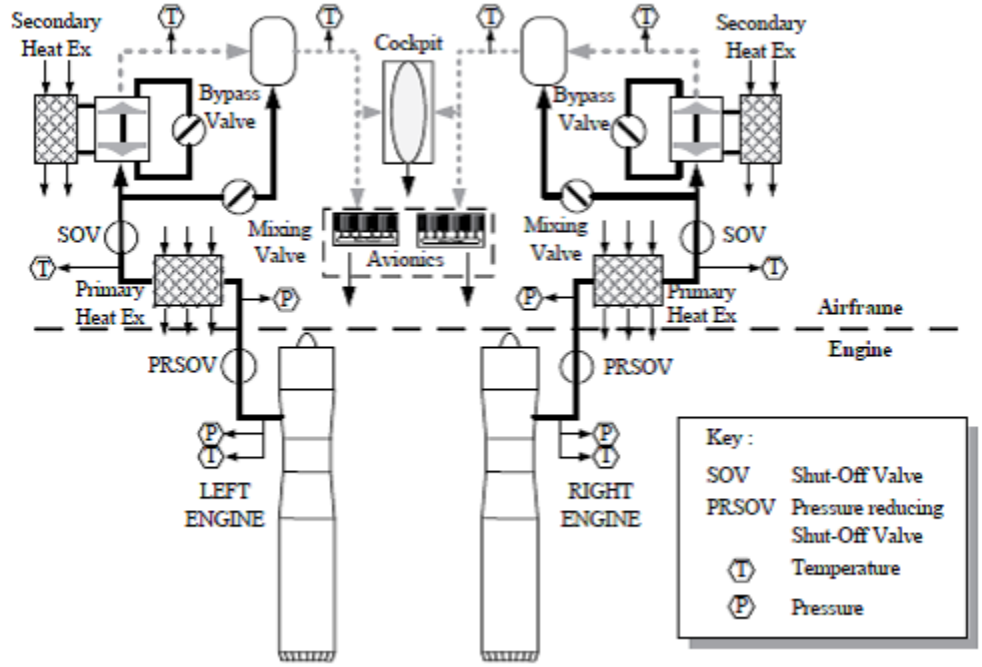

Figure 7. Typical military aircraft environmental control system (1)

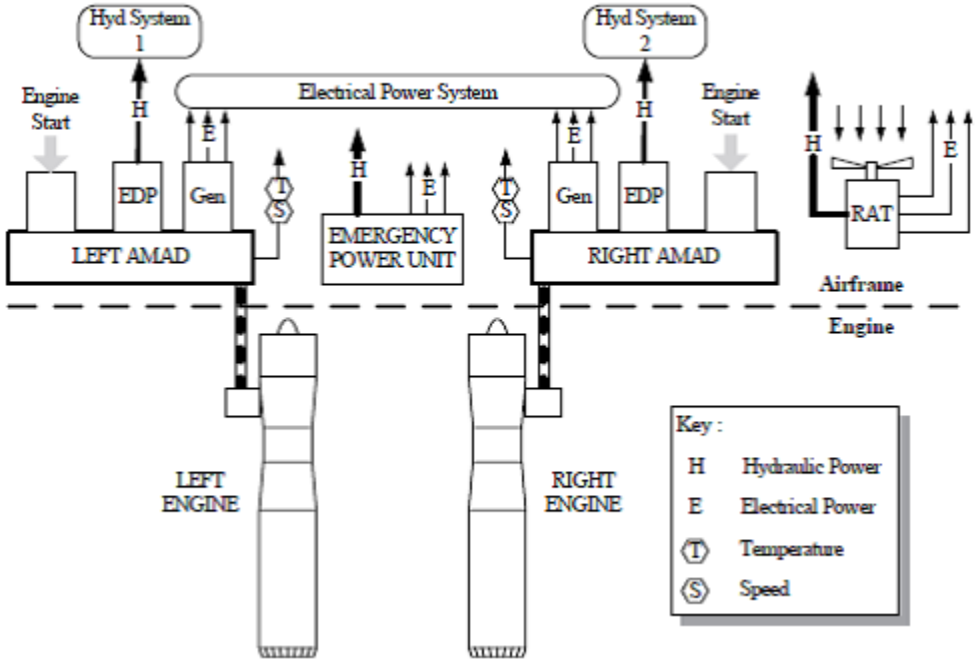

Figure 8. Typical military aircraft power generation system (1)

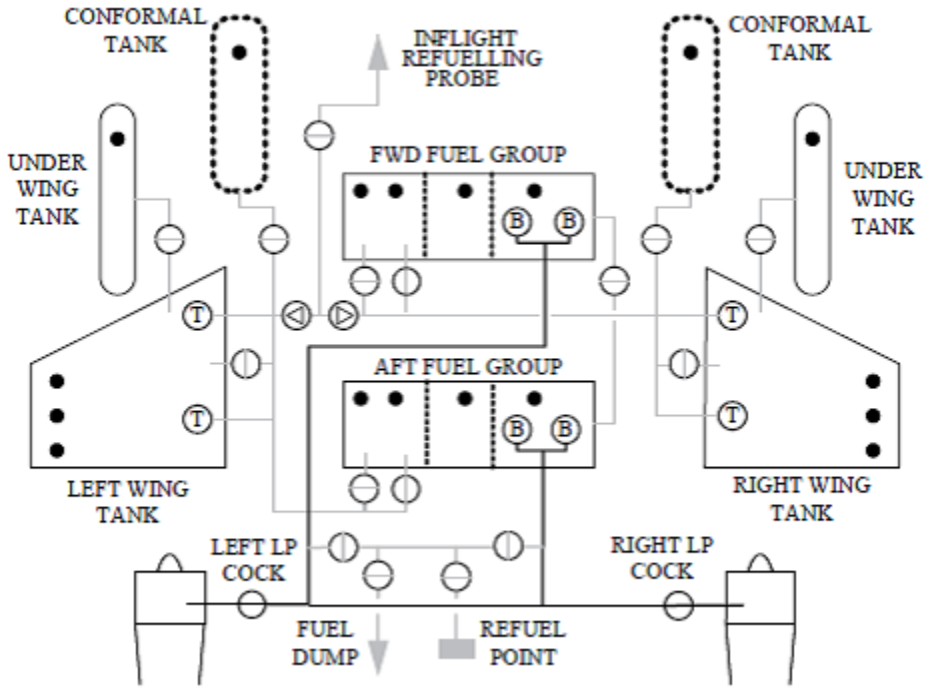

Figure 9. Typical military aircraft fuel system (1)

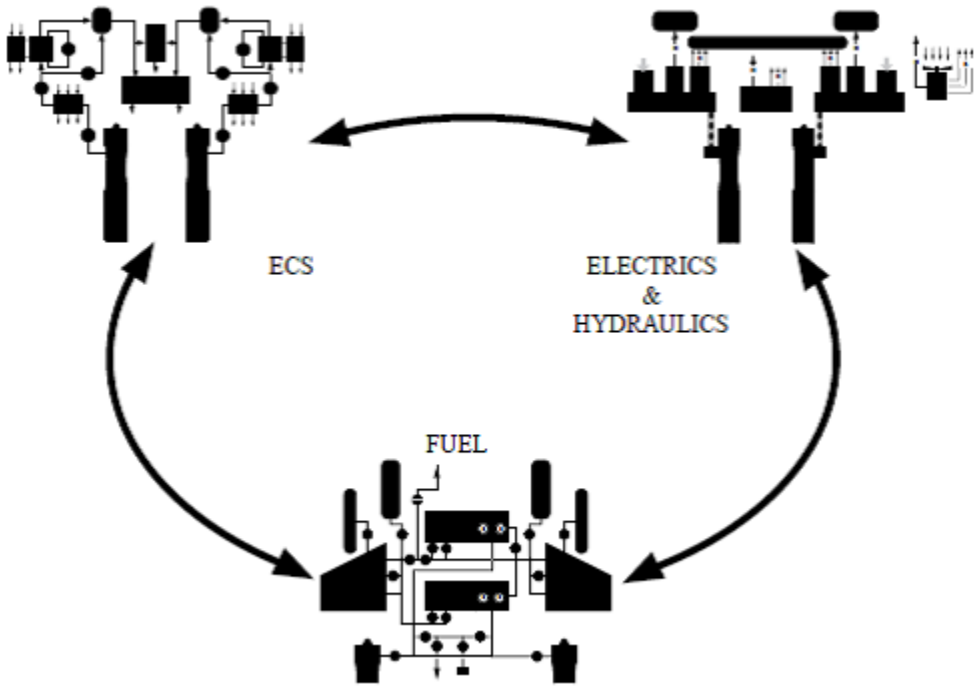

Figure 10. Typical military – system interaction (1)

All these systems are controlled by some sort of microelectronic devices. But what are the parts of aircraft electronic systems? Generally speaking, there are three main areas of avionics component development:

- Processors
- Memory
- Data buses

Each of these is defined by MIL-STD standard (for instance MIL-STD-1553 for data buses, MIL-STD-1750A for processors, etc.).

Digital processor devices became available in the early 1970s as 4-bit devices. By the late 1970s 8-bit processors had been superseded by 16-bit devices; these led in turn to 32-bit devices such as the Motorola 68000 which have been widely used on the European Fighter Aircraft and Boeing 777. (1)

Memory devices comprise two main categories: Read Only Memory (ROM) represents the memory used to host the application software for a particular function; as the term suggests this type of memory may only be read but not written to. Random Access Memory (RAM) is read-write memory that is used as program working memory storing variable data. Early versions required a power backup in case the aircraft power supply was lost. More recent devices are less demanding in this regard. (1)

The data buses are subsystems that transfer data between components inside a computer, or between computers. The ARINC 429 was the first data bus to be specified and widely used in civil aircraft, notably Boeing 757 and 767 and Airbus A300/A310 in the late 1970s and early 1980s. It was the introduction of standardized digital buses that made the biggest microelectronic impact on avionic systems.

All of the components are then placed on a printed circuit board (PCB), which is used to mechanically support and electrically connect all of the components.

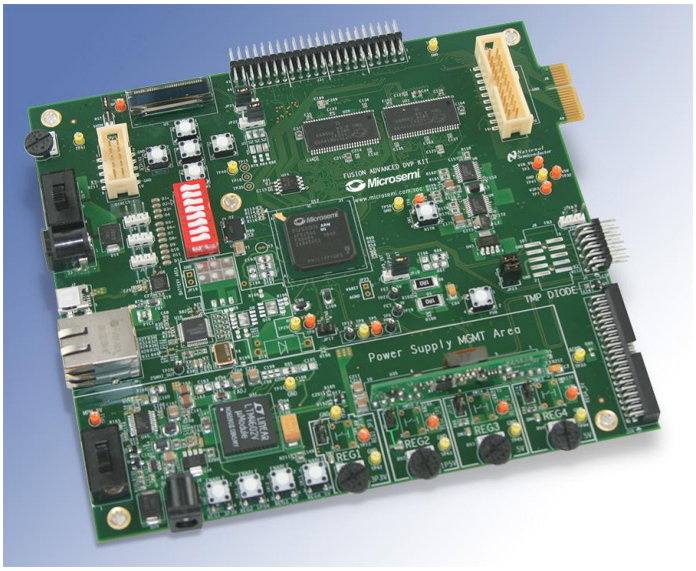

Figure 11. Microsemi Fusion Advanced Development Kit

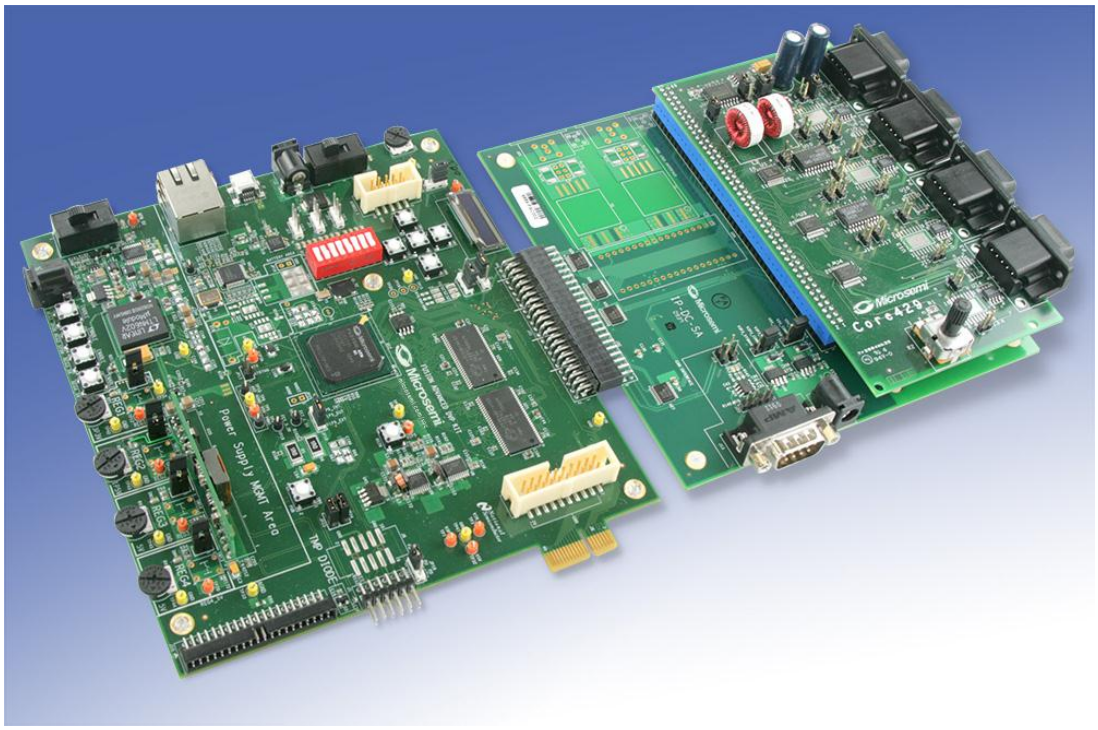

Figure 12. Microsemi Core429 Development Kit

The components are usually soldered to the PCB and these solders are usually the critical parts of the whole assembly when it comes to reliability. It is therefore necessary to ensure that these solders do not fail or reduce the possibility of failure to an acceptable rate.

2 Theoretical background

2.1 Time independent inelastic behavior

In order to determine the realistic behavior and the fatigue life of materials, it is necessary to include the inelastic behavior in the material model. Inelastic behavior can be divided into two groups, time independent, such as plasticity, and time dependent, such as creep.

Here the focus will be on the plasticity of materials, as plasticity (plastic strain range, inelastic strain energy density) is included in various fatigue models. These fatigue models will be mentioned and explained later in the text.

In most materials if the stress in the specimen is lower than the yield strength of the material, the material behaves elastically and strain is proportional to the stress in the specimen. If the stress in the specimen is greater than the yield stress, then the material exhibits elastic-plastic and no longer elastic behavior, and the stress-strain relationship becomes nonlinear. The following figure show a typical stress-strain curve. Both elastic and inelastic regions can be seen.

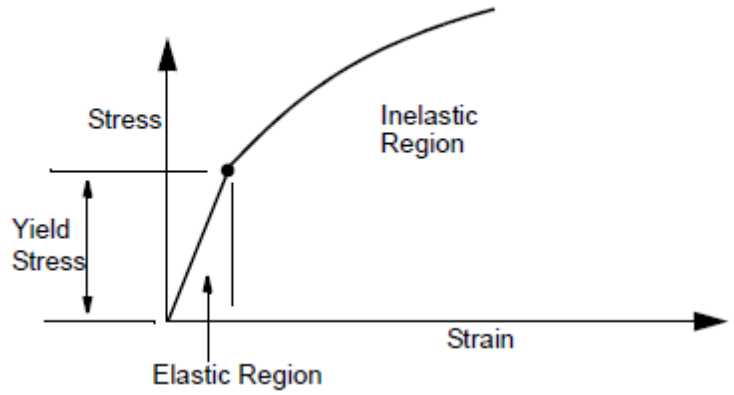

Figure 13. Stress-strain curve with elastic and inelastic regions (3)

Within the elastic region, the stress-strain curve shows linear relationship. This means, if the stress in the specimen is increased (loading) from zero point to σ_1 up to a maximum of yield stress (but not over it) and then decreased (unloading) back to zero, the strain in the specimen is also increased from zero to ε_1, and then returned back to zero. The elastic strain is completely recovered upon the release of stress in the specimen.

If case of loading and unloading occurs in the inelastic region (elastic-plastic region), the stress-strain relationship is different from the elastic region and is, as mentioned, nonlinear. The specimen is now loaded beyond yield point, where the total stress in the specimen is σ_2 and total strain is ε_2, upon release of the stress in the specimen the elastic strain ε_2^e is completely recovered, but the inelastic (plastic) strain ε_2^p remains.

The relationship can be seen in the following figure.

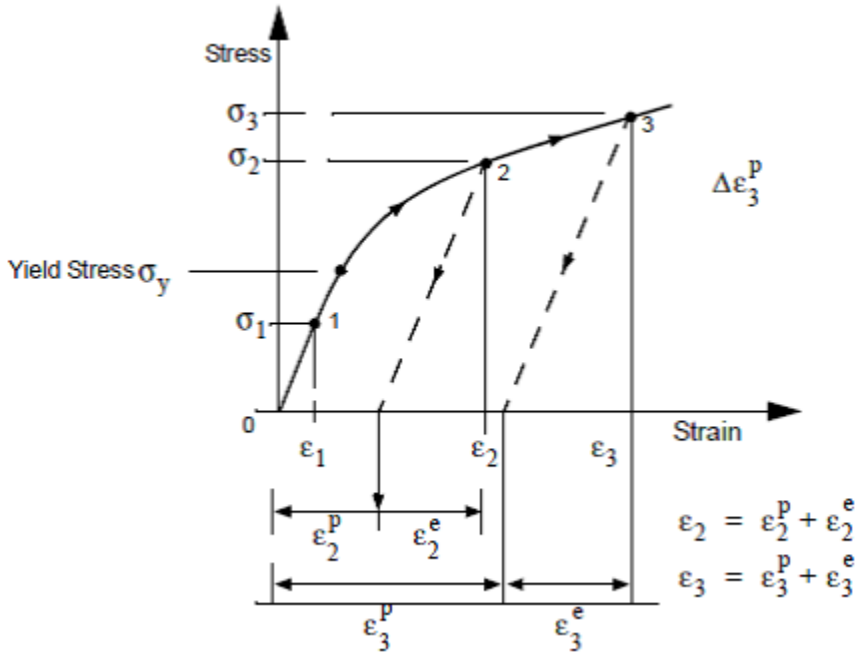

Figure 14. Stress-strain relationship during simple loading-unloading (uniaxial) test (3)

If the stress is increased to point 3 (meaning the σ_3 stress level is present in the specimen) and then unloaded to zero stress state, the plastic strain ε_3^p remains in the specimen. It can be seen the ε_3^p is greater than the ε_2^p. It can be concluded that in the inelastic region plastic strain remains permanently in the specimen upon the removal of the stress, and the amount od plastic strain remaining in the specimen is dependent upon the stress level at which the unloading starts (path-dependent behavior).

The stress-strain curve is usually shown for total quantities (total stress versus total strain). This can be replotted as total stress versus plastic strain, as shown in the following figure. The slope of the total stress versus plastic strain curve is defined as the workhardening slope (H) of the material. The workhardening slope is a function of plastic strain.

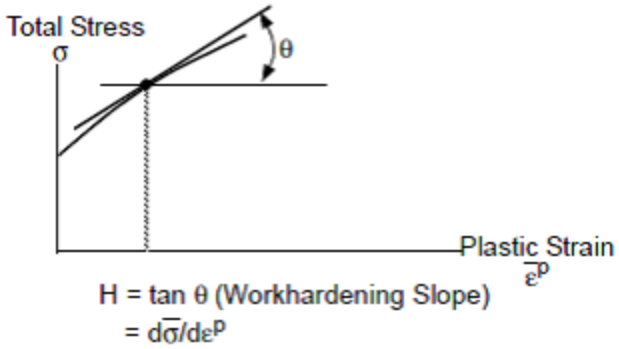

Figure 15. Workhardening slope (uniaxial stress) (3)

The stress-strain curve can be simplified to match certain cases:

- Bilinear representation – constant workhardening slope
- Elastic – perfectly plastic material – no workhardening
- Perfectly plastic material – workhardening and no elastic response
- Piecewise linear representation – multiple constant workhardening slopes
- Strain softening material

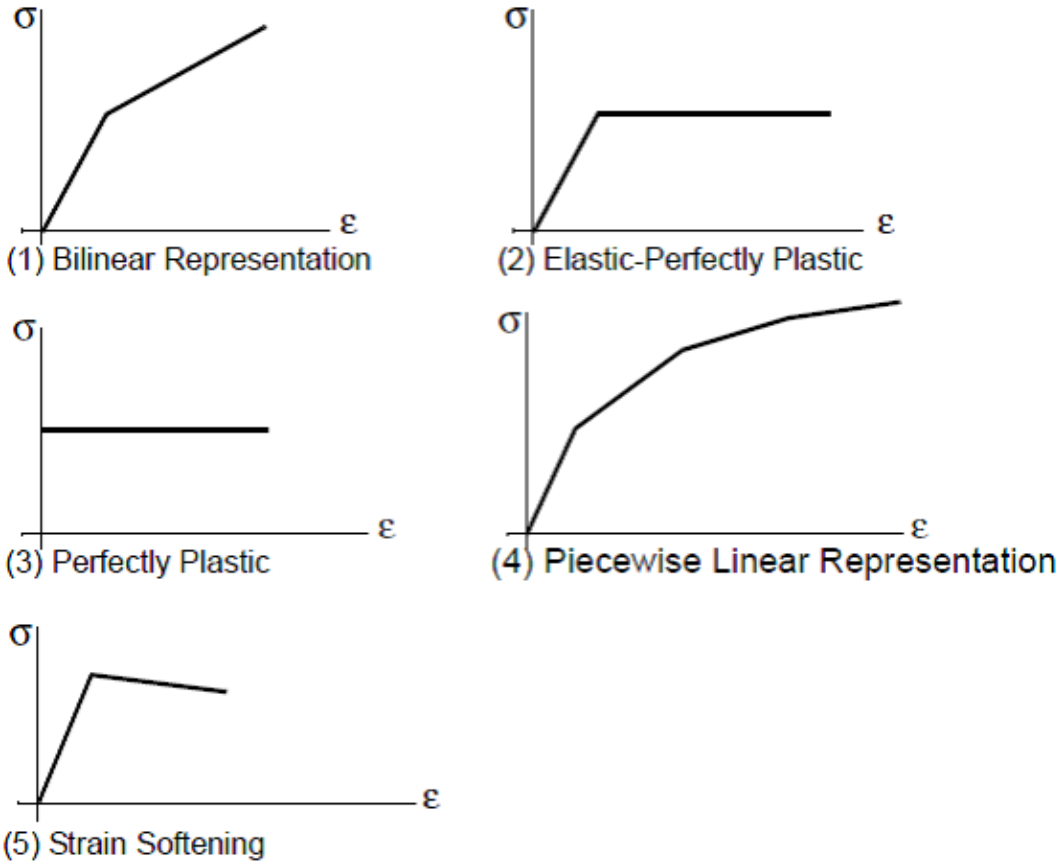

Figure 16. The stress-strain curve simplifications (3)

As stress in real structures is in most cases multiaxial, rather than uniaxial, it is necessary to reduce the stress using some sort of yield criterion. This will be discussed in the next chapter.

2.1.1 Yield criterion

In most materials there is a clear point (stress level) in stress-strain diagrams which separate elastic and inelastic regions. This point is called yield stress (or yield strength) of the material. The magnitude of the yield stress is obtained from a uniaxial test, but the stresses in structures are in most cases multiaxial. Therefore, it is necessary to somehow reduce the multiaxial stress to uniaxial. A measurement of yielding for the multiaxial state of stress is called the yield condition. There are many yield conditions, depending on how the multiaxial stress is represented. It can depend on all stress components, on shear components only, etc.

However, the most common is the Von Mises yield criterion, which covers most of the engineering materials. In this thesis the Von Mises criterion had been used.

2.1.1.1 Von Mises yield criterion

The Von Mises criterion states that yield occurs when the equivalent stress equals the yield stress (or strength) as measured in a uniaxial test. Figure 5. shows the von Mises yield surface in two and three dimensional stress space

For isotropic material for principal stresses (meaning $\tau_{xy} = \tau_{xz} = \tau_{yz} = 0$)

$$\bar{\sigma} = \sqrt{\frac{1}{2}[(\sigma_1 - \sigma_2)^2 + (\sigma_1 - \sigma_3)^2 + (\sigma_2 - \sigma_3)^2]}$$

For non-principal stresses

$$\bar{\sigma} = \sqrt{\frac{1}{2}\left[\left(\sigma_x - \sigma_y\right)^2 + \left(\sigma_y - \sigma_z\right)^2 + (\sigma_z - \sigma_x)^2 + 6\left(\tau_{xy}^2 + \tau_{yz}^2 + \tau_{xz}^2\right)\right]}$$

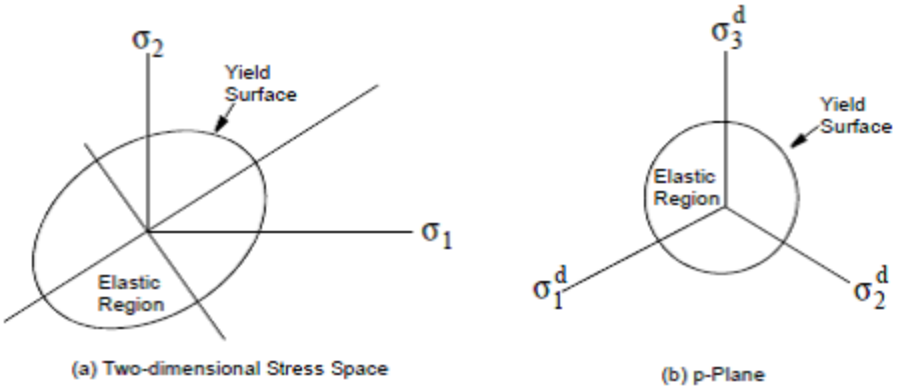

Figure 17. Von Mises yield surface (3)

The yield condition can also be expressed via deviatoric stresses as:

$$\bar{\sigma} = \sqrt{\frac{3}{2}\sigma_{ij}^{d}\sigma_{ij}^{d}}$$

Where σ_{ij}^{d} is the deviatoric stress defined as

$$\sigma_{ij}^{d} = \sigma_{ij} - \frac{1}{3}\sigma_{kk}\delta_{ij}$$

2.1.1.2 Strain or Work hardening

As mentioned before, the workhardening slope is defined as the slope of the stress-plastic strain curve. The workhardening slope relates the incremental stress to incremental plastic strain in the inelastic region and defines the conditions of the subsequent yielding.

2.1.1.2.1 Isotropic hardening

The isotropic hardening rule assumes that the center of the yield surface remains stationary in the stress space, but the size (radius) of the yield surface expands due to the workhardening. This can be seen in the figure 18.

The specimen is first loaded from stress free state (point 0) to initial yield point 1. It is then loaded to point 2. Then, it is unloaded from 2 to 3 and subsequently loaded from 3 to 2. All of this occurs on the elastic slope *E* (Young's modulus). Finally, the specimen is plastically loaded again from 2 to 4 and then elastically unloaded from 4 to 5. Reverse plastic loading occurs between 5 and 6.

The stress at 1 is equal to the initial yield stress (which will increase later) σ_Y and the stresses at points 2 and 4 are larger than σ_Y due to the workhardeing. During the unloading the stress state remains elastic (point 3), even though permanent plastic strain is present. If the specimen continues to be unloaded and then reversely loaded, the new stress level will reach the reverse

yield point. The isotropic hardening rule stated that the reverse yield point occurs at current stress level in the reversed direction. If the specimen is loaded from point 3 to point 4 (stress level σ_4), the reverse yield can only occur at a stress level of $-\sigma_4$ (point 5).

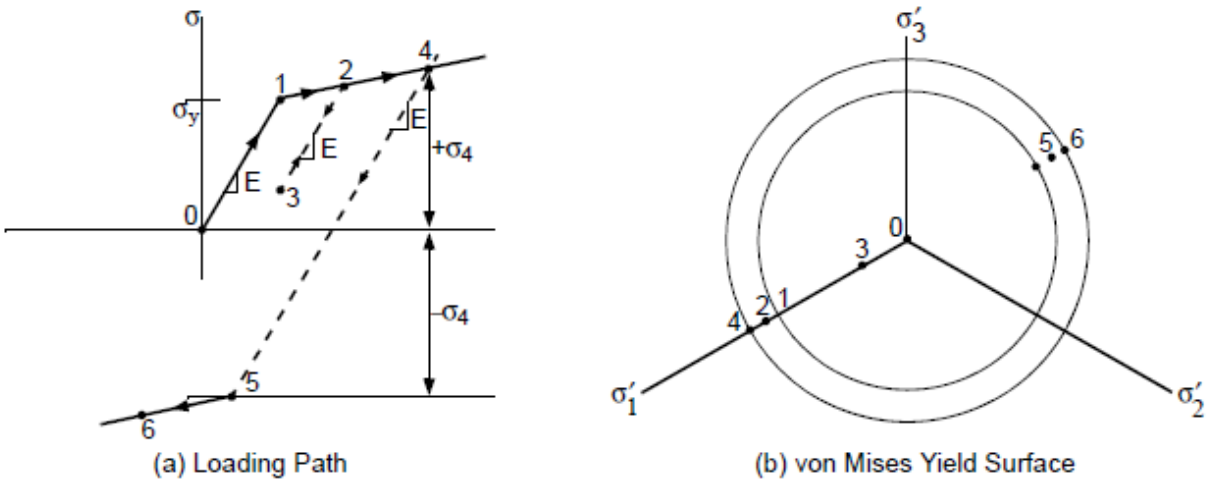

Figure 18. Isotropic hardening (3)

Since isotropic workhardening is not accurate for a number of materials in case of unloading (as in cyclic loading problems), alternative workhardening rules are used; kinematic workhardening and combined workhardening.

2.1.1.2.2 Kinematic hardening

Unlike isotropic hardening, in the kinematic hardening rule, the von Mises yield does not change in size or shape, but the center of the yield surface moves in the stress space.

The loading path of the uniaxial test is shown in the Figure 19. Schematic of kinematic hardening rule . The specimen is loaded in the following order: from stress free state (point 0) to initial yield (point 1), point 2 (loading), 3 (unloading), 2 (reloading), 4 (loading), 5 and 6 (unloading). As in isotropic hardening, stress at 1 is equal to the initial yield stress σ_Y, and stresses at 2 and 4 are higher than σ_Y, due to the workhardening. Point 3 is elastic and reverse yield point takes place at point 5. Under the kinematic hardening rule, the reverse yield occurs at the level of $\sigma_5 = (\sigma_4 - 2\sigma_Y)$, rather than at the stress level $-\sigma_4$. Similarly, if the specimen is loaded to a higher stress level σ_7 (point 7), and then unloaded to the subsequent yield point 8, the stress at point 8 is $\sigma_8 = (\sigma_7 - 2\sigma_Y)$. If the specimen is unloaded from a (tensile) stress state (such as point 4 and 7), the reverse yield can occur at a stress state in either the reverse (point 5) or the same (point 8) direction.

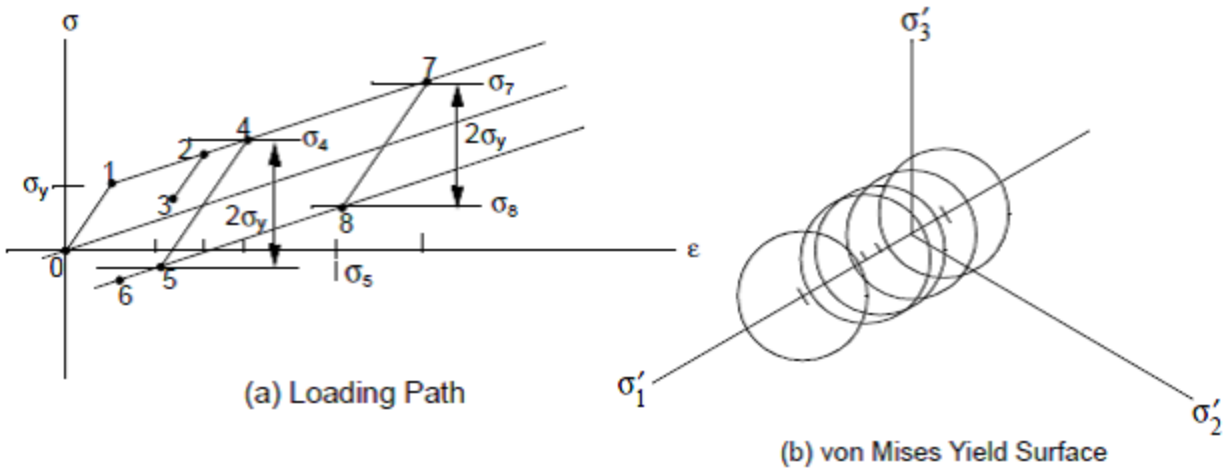

Figure 19. Schematic of kinematic hardening rule (3)

2.1.1.2.3 Combined hardening

The combined hardening is depicted in the Figure 10. and shows a material with highly nonlinear hardening. Here the initial hardening is assumed to be almost entirely isotropic, but after some plastic straining, the elastic range attains essentially constant value (that is, pure kinematic hardening). The basic assumption of the combined hardening model is that such behavior is reasonably approximated by a classical constant kinematic hardening constraint, with the superposition of initial isotropic hardening. The isotropic hardening eventually decays to zero as a function of the equivalent strain. The total equivalent plastic strain $\bar{\varepsilon}^p$ is defined as

$$\bar{\varepsilon}^p = \int \dot{\bar{\varepsilon}}^p \, dt = \int \sqrt{\frac{2}{3} \dot{\varepsilon}_{ij}^p \dot{\varepsilon}_{ij}^p} dt$$

This implies a constant shift of the center of the elastic domain, with a growth of elastic domain around the center until pure kinematic hardening is attained. In this model there is a variable proportion between the isotropic and kinematic contributions that depends on the extent of the plastic deformation (as measured by $\bar{\varepsilon}^p$).

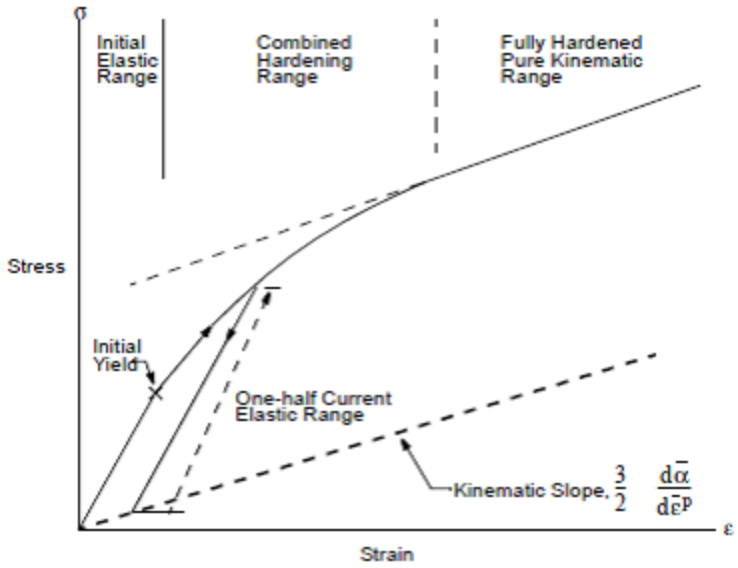

Figure 20. Uniaxial behavior of the combined hardening model (3)

2.2 Vibrations of Single Degrees of Freedom system

In mechanical engineering vibrations are mechanical oscillations around equilibrium point. They may be periodic (follow a function that repeats its values in regular or periodic intervals, such as sine function) or random. While vibrations can be desirable at certain occasions, more often than not they are considered undesirable and attempts are made to minimize their effect.

Vibrations can be roughly divided into two groups; free vibrations and forced vibrations.

Free vibrations occur when a mechanical system is set off with an initial input and then allowed to vibrate freely. The mechanical system will then vibrate at its natural frequency and, if damping is present, will damp down to zero.

Forced vibration is when alternating force (or motion) is applied to the mechanical system. These can be engine induced vibrations in the aircraft, or vibrations induced by the aerodynamic forces.

As stated in MIL standard, when talking about periodic (for instance sine vibrations) and random vibrations, it is "necessary to know that sine and random characterization of vibration are based on distinctly different set of mathematics. In order to compare the effects of give random and sine vibration on material, it is necessary to know the details of material dynamic response. A general definition of equivalence is not feasible.

Often, attempts are made to compare the peak acceleration of sine to the *rms* (root mean square) acceleration of random. The only similarity between these measures is the dimensional units that are typically acceleration in the standard gravity units. Peak sine acceleration is the maximum acceleration at the one frequency. Random *rms* is the square root of the area under a spectral density curve. These are not equivalent."

The vibration frequency spectrum for airplanes will vary from about 3, to about 1000 Hz, with acceleration levels that can range from about 1 G to about 5 G peak. The highest accelerations appear to occur in the vertical direction in the frequency range of about 100-400 Hz. The lowest accelerations appear to occur in the longitudinal direction, with maximum levels of about 1 G in the same frequency range. (4)

For helicopters, the frequency spectrum will vary from about 3 to about 500 Hz and acceleration will range from about 0.5 to about 4 G. The highest accelerations appear to occur in the vertical direction at frequencies near 500 Hz. The displacements at low frequencies are very large, with values of about 5 mm. double amplitude at about 10 Hz. (4)

Missiles have the highest frequency range in this group, with values that generally go up to 5000 Hz. The lower frequency limit is about 3 Hz, and this appears to be due to bending modes in the airframe structure. (4)

Acceleration levels range from about 5 to about 30 G peak, with the maximum levels occurring during power-plant ignition at frequencies above 1000 Hz. The vibration environment in supersonic airplanes and missiles is actually more random in nature than it is periodic. However, sinusoidal vibration tests are still being used to evaluate and to qualify electronic equipment that will be used in these vehicles.

Because the forcing frequencies in airplanes and missiles are so high, it is virtually impossible to design resonance-free electronic systems for these environments.

2.2.1 Mathematical fundamentals

To begin the analysis of the vibrating system, the first step is to investigate the free vibrating mass-spring-damper with negligible damping and with no external force applied (i.e. free vibrations). In vibration analysis the spring is considered to be ideal, meaning no mass and energy dissipation (i.e. no spring damping).

2.2.1.1 Free vibrations

The force applied to the mass by the spring is proportional to the displacement *u* and spring stiffness constant *k.*

$$F_s = -ku$$

The negative sign indicates that the spring is opposing the motion of the mass attached to it.

The force of the mass is determined by Newton's second law of motion

$$F_m = ma = m\frac{d^2u}{dt^2} = m\ddot{u}$$

The sum of forces generates the ordinary differential equation of the system.

$$m\ddot{u} + ku = 0$$

The equation can be rearranged

$$\ddot{u} + \frac{k}{m}u = 0$$

Where

$$\omega_n = \sqrt{\frac{k}{m}}$$

Is called undamped natural frequency and is one of the most important quantities in vibration analysis.

The vertical displacement can be represented by the equation

$$u = u_0 sin\omega t$$

The velocity is the first derivative

$$v = \dot{u} = \frac{du}{dt} = \omega u_0 \cos \omega t$$

And the acceleration is the second derivative

$$a = \ddot{u} = \frac{d^2u}{dt^2} = -\omega^2 u_0 \sin \omega t$$

The negative sign indicates that acceleration acts in the direction opposite to the displacement.

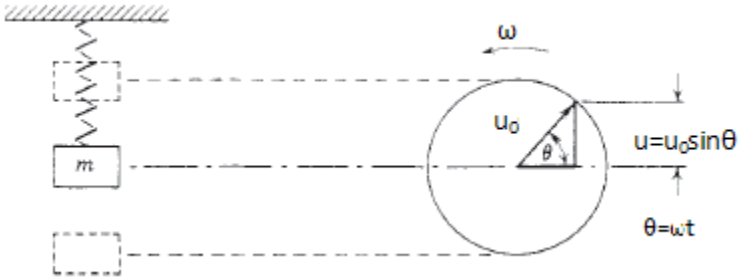

Figure 21. One DOF undamped system. The rotating vector describes the harmonic motion (4)

The maximum acceleration will occur when $\sin \omega t = 1$,

$$a_{max} = \omega^2 u_0$$

The equation can be rearranged and expressed in gravity units (G), by dividing the maximum acceleration with the acceleration of gravity,

g=9.81 m/s^2

Also, the frequency can be expressed as

$$\omega = 2\pi f$$

Substituting into the equation yields

$$G = \frac{a_{max}}{g} = \frac{4\pi^2 f^2 \mathrm{u}_0}{9.81}$$

2.2.1.2 Forced vibrations with viscous damping

Consider a harmonic force $P_0 cos\omega t$ acting on a damped spring mass system.

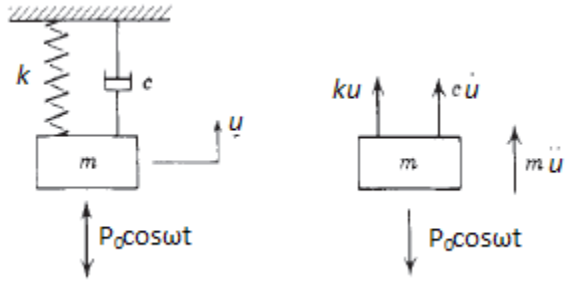

Figure 22. Forced vibrations acting upon a damped system (4)

The differential equation of motion with external force acting is

$$m\ddot{u} + c\dot{u} + ku = P_0 cos\omega t$$

The maximum displacement u_0 can be expressed in terms of the maximum imposed force P_0.

$$u_0 = \frac{P_0}{\sqrt{[(k - m\omega^2)^2 + (c^2\omega^2)^2]}}$$

Dividing the numerator and denominator with stiffness K of the above equation yields

$$u_0 = \frac{P_0}{k} \frac{1}{\sqrt{[(1 - R_\Omega^2)^2 + (2R_c R_\Omega)^2]}}$$

The expression P_0/k represents the static deflection $u_{st,}$ this yields

$$u_0 = u_{st} \frac{1}{\sqrt{[(1 - R_\Omega^2)^2 + (2R_c R_\Omega)^2]}}$$

The u_0/u_{st} ratio represents system amplification which should not be confused with system transmissibility

$$A = \frac{u_0}{u_{st}} = \frac{1}{\sqrt{[(1 - R_\Omega^2)^2 + (2R_c R_\Omega)^2]}}$$

The plot shows dynamic amplification ratio A against frequency in the Fig. 3

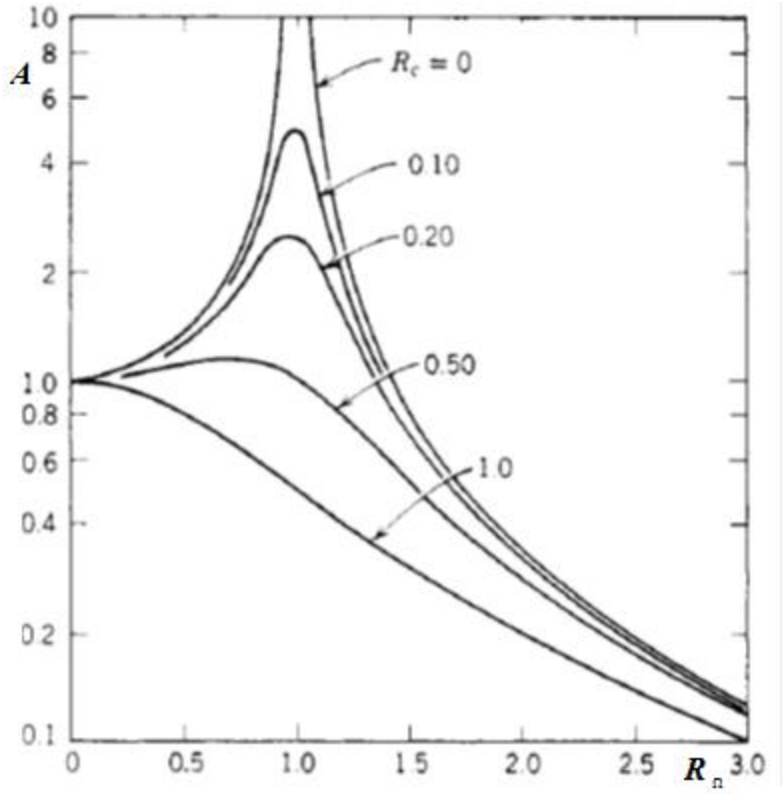

Figure 23. Dynamic amplification curve (4)

Where the R_Ω is equal to

$$R_\Omega = \frac{\omega}{\omega_n}$$

In order to determine the transmissibility it is necessary to determine the maximum output force F_0. The instantaneous magnitude of the force experienced by the support is the vector sum of the spring force and the damper force. These two forces have a 90^o phase angle between them, so the force becomes

$$F_0 = u_0\sqrt{(k^2 + c^2\omega^2)}$$

The system transmissibility Q, which represents the ratio of the maximum output force F_0 to the maximum input force, P_0 can be determined by dividing the numerator and the denominator by k and substituting into the maximum deflection equation. This yields

$$F_0 = \frac{P_0\sqrt{(k^2 + c^2\omega^2)}}{\sqrt{[(k - m\omega^2)^2 + (c^2\omega^2)^2]}}$$

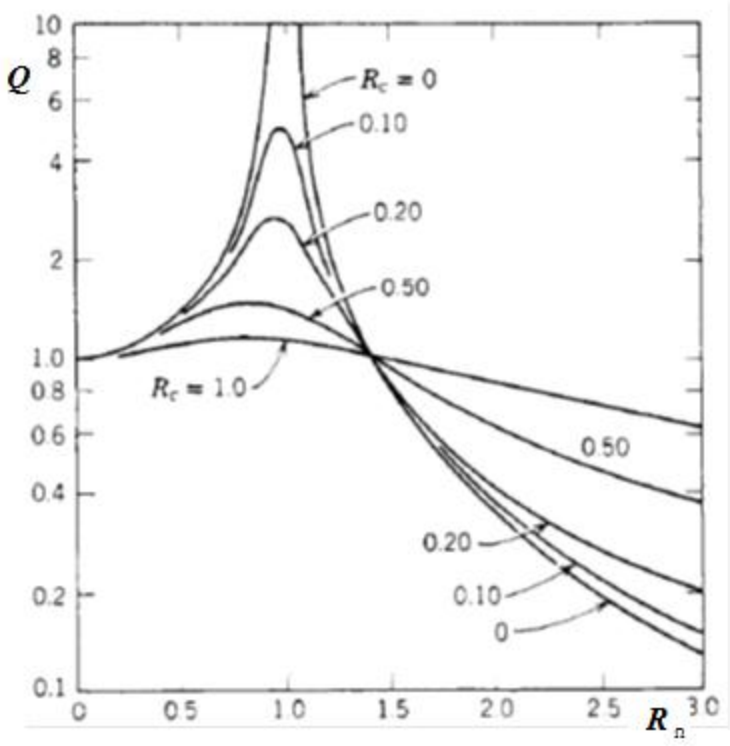

Figure 24. Transmissibility curve (4)

As mentioned before, the transmissibility is defined as F_0/P_0. Written in non-dimensional form, the equation yields

$$Q = \frac{F_0}{P_0} = \sqrt{\frac{1 + (2R_c R_\Omega)^2}{(1 - R_\Omega^2)^2 + (2R_c R_\Omega)^2}}$$

Extensive test data on PCBs, with various edge restrains, indicate that many epoxy fiberglass circuits boards, with closely spaced electronic components, have a transmissibility that can be approximated by equation (4)

$$Q = \sqrt{f_n}$$

3 Solder joint fatigue

Today, electronic assemblies play a vital role in the aerospace industry. They serve as aircraft communication devices, navigation, flight control systems, weather systems, mission or tactical avionics for military aircraft, etc. These assemblies are exposed to a wide range of environmental loads, depending on their location within the aircraft. These can be thermal loads, vibrations, shock, etc., or any combination of those. Unexpected failure of electronic systems results in safety risks, damage and consequential costs. High reliability and availability of electronic systems add to their economic and ecological benefits.

As per USAF report (4) 55% of all failures are attributed to thermal cycling and 20% to vibration. While the information is available on thermal cycling failures and, to a lesser extent vibration induced failures (especially on lead-free solders), the information on combined vibration and thermal cycling is scarce. It is important to mention, that while both thermo-mechanical and vibration loads cause cracks on the solder joint, the damage mechanisms are completely different. Therefore, it is necessary to consider and analyze them separately, before the analysis of the combined loading can be given.

In thermal fatigue the damage is cause by plastic deformation. The cyclic deformation is imposed as the result of the constrained differential expansion within a solid caused by temperature gradients induced during alternate heating and cooling. Thermal fatigue is typically a low-cycle fatigue problem (less than 10^4 $N_{f,TC}$ thermal cycles to failure).

On the other hand, in the vibration induced fatigue, the loads which damage the electronic assemblies are relatively small and induce stresses which are usually under the yield stress. The damage is caused by repeated elastic deformations which after a high number of cycles damage the assembly. This kind of damage is called High Cycle Fatigue (HCF) and occurs after more than 10^5 $N_{f,Vib}$ cycles (vibration cycles to failure).

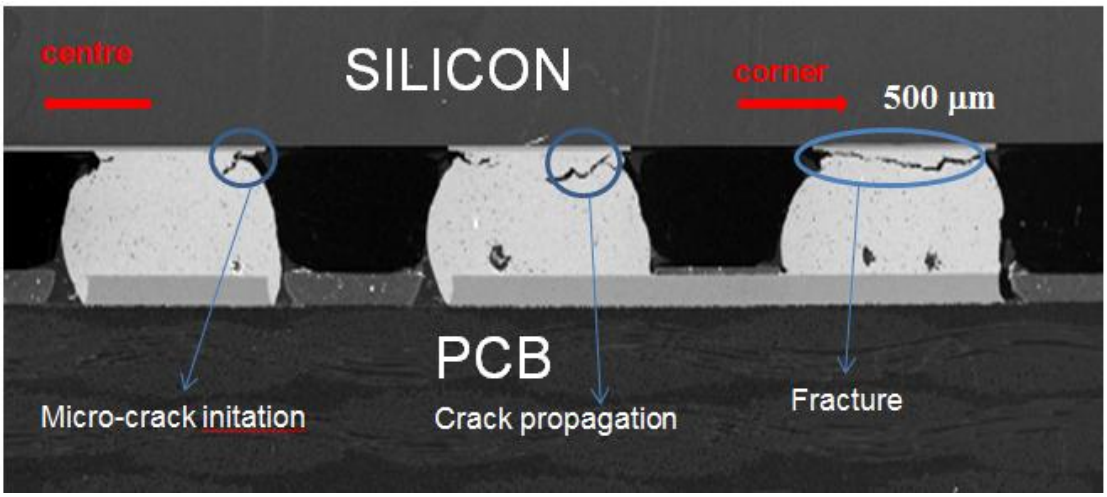

Figure 25. Example of crack propagation under thermal loading (5)

3.1 Low Cycle Thermal Fatigue

As already mentioned, in thermal fatigue the damage is caused by plastic deformation. This deformation is induced by the mismatch of thermal expansion coefficients between the components. Apart from temperature, frequency also plays an important part on LCF behavior (for LCF these are usually within the range 10^{-3} – 1 Hz in an uniaxial tension – compression loading test). The solder is softer than other components, so most of the cyclic stresses and strains take place in solder. Therefore, fatigue failure, especially thermally induced low cycle fatigue (LCF) failure, is likely to occur in the solder. There are a number of approaches used for analyzing thermal fatigue; strain-based, energy-based analysis, etc.

The Low Cycle fatigue region is shown in the following figure

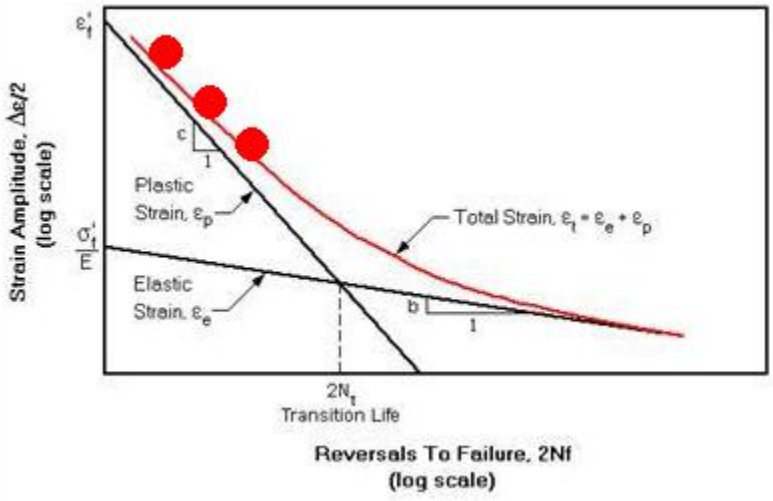

Figure 26. Low Cycle fatigue (LCF region is denoted by the red dots)

Coffin-Manson fatigue model

For strain-based analysis, Coffin-Manson fatigue model is widely used for low cycle fatigue analysis. The total number of cycles to failure $N_{f,TC}$ is dependent on the plastic strain range $\Delta\varepsilon_p$ (or plastic strain amplitude $\frac{\Delta\varepsilon_p}{2}$, depending which formulation is used), the fatigue ductility coefficient *C*, and the fatigue ductility exponent *m*. This plastic strain range is equivalent to the width of the hysteresis loop. For the same strain range, the plastic strain range increases with increasing temperature, while the stress range $\Delta\sigma$ decreases with the increasing temperature. The relation between the plastic strain range and the number of cycles to failure is given below.

$$N_{f,TC}^{m}\Delta\varepsilon_p = C$$

It is reported by Kanchanomai et al (6) that fatigue ductility exponents for different frequencies are similar, while the fatigue ductility coefficients increase with increasing frequency and decreasing temperature.

The influence of frequency on fatigue life can be described in terms of a frequency-modified Coffin-Manson relationship (6)

$$\left(N_{f,TC}\nu^{k-1}\right)^{\alpha}\Delta\varepsilon_p = C$$

Where ν and k are the frequency and frequency exponent from the fatigue life-frequency relationship.

Smith-Watson-Topper model

The Smith-Watson-Topper is another model (6) for Low Cycle Fatigue. It assumes that fatigue life depend on the product $\sigma_{max}\Delta\varepsilon_T$

$$(\sigma_{max}\Delta\varepsilon_T)N_{f,TC}^{n} = d$$

Where σ_{max} is the maximum stress, $\Delta\varepsilon_T$ is total strain range, *n* is ductility exponent and *d* is the fatigue ductility coefficient. It is reported by Kanchanomai et al (6) that the fatigue ductility exponents for different temperatures and frequencies are basically similar, while the fatigue ductility coefficient increases with decreasing temperature and increasing frequency.

Morrow model

The Morrow model, (6) is energy based model (plastic strain energy density-life model). The plastic strain energy density can physically be described as distortion energy associated with the change in shape of a element volume. It can be calculated as inner area (W_p) of the stress-strain hysteresis loop for uniaxial fatigue test. The fatigue life is defined as

$$N_{f,TC}^{m}W_p = C$$

Where W_p is the plastic strain energy density, $N_{f,TC}$ is the number of cycles to failure, *m* is fatigue exponent, while *C* is fatigue coefficient. The fatigue exponent for different temperatures and frequencies are similar, while the fatigue coefficient increases with decreasing temperature and increasing frequency. In order to describe the effect of frequency, a frequency-modified Morrow energy model is introduced by Kanchanomai et al (6).

The model predicts fatigue life in terms of the plastic strain energy density W_p

$$\left(N_{f,TC}\nu^{k-1}\right)^{m}W_p = C$$

Where ν and k are the frequency and frequency exponent from the fatigue life-frequency relationship. Another proposed Morrow model by Kanchanomai et al (6) is a flow stress

modified frequency model, in which both temperature-dependent and frequency-dependent material properties were introduced into the plastic strain energy density model

$$\left(N_{f,TC}\nu^{k-1}\right)^{m}\frac{W_p}{2\sigma_f}=C$$

Where σ_f is flow stress (averaged value between the yield point and the highest stress of hysteresis loop) and *m* and *C* are constants.

The fatigue damage due to the thermal cycling is equal to the reciprocal of the life

$$D_{th}=\frac{1}{N_{f,TC}}$$

3.2 Vibration induced High Cycle Fatigue (HCF)

As already mentioned, vibration induced high cycle fatigue differs from low cycle fatigue in a number of ways. The damage is usually brought by elastic deformations which after a high number of cycles (more than 10^4 cycles) lead to solder failure. This can be seen in the following figure

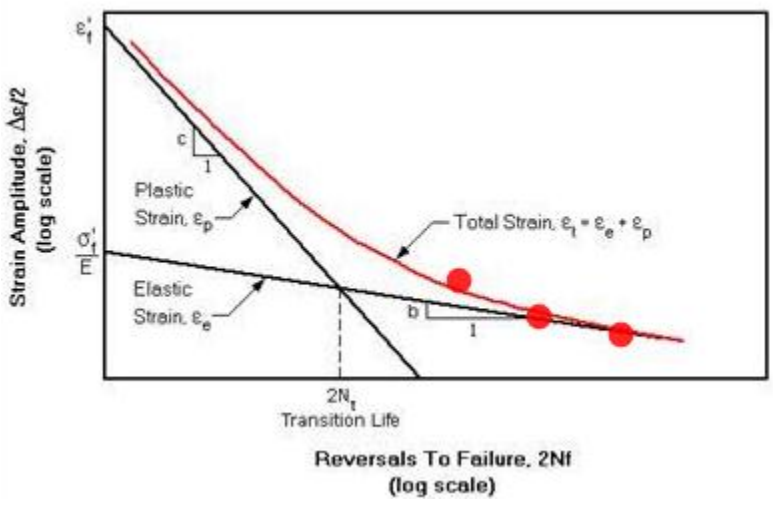

Figure 27. High cycle fatigue (HFC region is denoted by red dots)

The Basquin relation is used to determine the cycles to failure in the High Cycle fatigue.

$$N_{f,vib}=\frac{1}{2}\left(\frac{\sigma_a}{\sigma_f'}\right)^{\frac{1}{b}}$$

Where N_f denotes the number of cycles to failure, σ_a the maximum of the repeating stress, σ_f' the fatigue strength coefficient, and b the fatigue strength exponent (both of which are material constants). This equation can be rearranged into

$$\varepsilon_a = \frac{\sigma_f'}{E}\left(2N_{f,vib}\right)^b$$

As mentioned before, the absence of plastic material behavior is a prerequisite for the proper use of the Basquin equation, since the use of maximum stress σ_a as a damage model is not capable of describing a possible plastic material response. On the other hand, weak solder material behavior and localized stress accumulation due to the geometry of the components (and the PCB) can lead to plastic deformations. This can also occur in case of random vibrations, where certain amplitude might cause plastic deformations. These possibilities must be taken in consideration when Basquin equation is used.

Another approach by Eckert et al (7) is to assume that vibration fatigue life is limited to a combination of both plastic and elastic deformations.

The Coffin-Manson-Basquin relationship is an approach that takes both plastic and elastic strains into the account, when calculating the fatigue life.

$$\frac{\Delta\varepsilon_{tot,vib}}{2} = \frac{\Delta\varepsilon_{el}}{2} + \frac{\Delta\varepsilon_{pl}}{2} = \frac{\sigma_f'}{E}\left(2N_{f,vib}\right)^b + \varepsilon_f'\left(2N_{f,vib}\right)^c$$

Where $\Delta\varepsilon$ is the strain range (total, elastic or plastic) of one cycle, σ_f' the fatigue strength coefficient, b the fatigue strength exponent, ε_f' the fatigue ductility coefficient, and *c* the fatigue ductility exponent (all four coefficients are material constants). Also, knowing the fundamental frequency of the system, the $N_{f,vib}$ can be converted to TTF (Time-to-Failure) for the vibration load.

As in low cycle thermal fatigue, the fatigue damage is equal to the reciprocal of the life

$$D_v = \frac{1}{N_{f,vib}}$$

3.3 Combined Vibration and Thermal cycling

In many cases, electronic assemblies are under combined thermal and vibration loads. In this case, the situation becomes much more complicated as two different types of loading must be combined and assessed. Also, a new fatigue model must be developed to take in the account the effects of both thermal and vibration loadings. This task is not easy, as it combines both Low and High cycle fatigue.

An attempt is made by Eckert et al (7) with modifying the Coffin-Manson-Basquin relationship. In order to estimate an expected lifetime for combined loads the single loads can be superposed linearly without accounting for interaction effect or using an incremental damage superposition

approach. Then the mean stresses as induced by thermal cycling are accounted for by extending the equation as follows:

$$\frac{\Delta\varepsilon_{tot,vib}}{2} = \frac{\Delta\varepsilon_{el}}{2} + \frac{\Delta\varepsilon_{pl}}{2} = \frac{\sigma_f' - \sigma_m(T)}{E}\left(2N_{f,vib}\right)^b + \varepsilon_f'\left(2N_{f,vib}\right)^c$$

The equation needs to be solved numerically.

With knowing the necessary frequencies, the $N_{f,vib}$ and $N_{f,TC}$ can be converted to $TTF_{Vibration}$ and TTF_{TC}. Here, the $TTF_{Vibration}$ is superposed with TTF_{TC} by using

$$TTF = \frac{1}{\frac{1}{TTF_{TC}} + \frac{1}{TTF_{vib}}}$$

This gives total time to failure.

4 Fatigue analysis of a Printed Circuit Board

4.1 Vibration analysis of a rectangular plate

In this chapter a short introduction in the vibration of plates will be given. The goal is to show which parameters of plates (or PCBs) influences the natural frequencies of the plates and therefore the other factors, for instance transmissibility.

Only basic equations will be given here. Complete theory can be found in various literature. Timoshenko et al (8) and Chakraverty (9) are recommended here.

The equation of motion for transverse vibration is

$$D\nabla^4 w + \rho h \frac{\partial^2 w}{dt^2} = 0$$

where

w is the transverse displacement of the plate

ρ – density of the material of the plate

h – thickness of the plate

D – flexular rigidity

∇^4 - biharmonic operator

$$\nabla^4 w = \frac{\partial^4 w}{\partial x^4} + 2\frac{\partial^4 w}{\partial x^2 \partial y^2} + \frac{\partial^4 w}{\partial y^4}$$

Also, $\nabla^4 w = \nabla^2(\nabla^2 w)$ where ∇^2 is the Laplacian operator.

Flexular rigidity of the plate is defined as

$$D = \frac{Eh^3}{12(1-\nu^2)}$$

where

E – Young's modulus

ν - Poisson's ratio

h – thickness of the plate

From the previous equations it is possible to obtain the frequencies of plates with various boundary conditions. For simply supported plate the equation is

$$\omega_{mn} = \pi^2 \left[\left(\frac{m}{a}\right)^2 + \left(\frac{n}{b}\right)^2 \right] \sqrt{\frac{D}{\rho h}}$$

Where *a* and *b* are plate dimensions and *m,n*=1,2,3....

This equation (dividing by 2π) can be used to analytically check the FEM model. The comparison can be seen in the following table.

Eigenfrequency [Hz]	**Analitical solution**	**FEM**
1st mode	3744	3813
2nd mode	9362	9197
3rd mode	9326	9197

Table 1 Comparison of analytical and FEM results for simply supported PCB

As it can be seen, the difference between the two methods is less than 2%. Also, the CSP (along with four solders) has negligible effect on eigenfrequencies.

One of the main assumptions is that the mass (or components) is equally distributed along the PCB. If this is not the case, meaning there is a mass concentration anywhere on the board, this equation cannot be used.

Also, in case of boundary conditions other than simply supported, the procedure is far more complicated and other methods of obtaining natural frequencies are recommended.

One of the most common boundary condition is the case of the board with two clamped and two free edges. Such case can be found on mechanical shakers which are used for vibration testing However, in this case it is necessary to use empirical equations, as it is impossible to solve the equation analytically Good source of empirical equations can be found in (10).

For a rectangular plate with two clamped and two free edges the eigenvalue of the first mode can be calculated by the following equation

$$\omega = \frac{22.17}{a^2 \sqrt{\frac{\rho h}{D}}}$$

As in the previous case, this equation can be used to analytically check the FEM model, details of which can be found in chapter 0. The comparison can be seen in the following table.

Eigenfrequency [Hz]	**Analitical solution**	**FEM**
1st mode	4206	4205

Table 2 Comparison of analytical and FEM results for PCB with two clamped and two free edges

Figure 28. First eigenfrequencies for a rectangular plate with two clamped and two free edges shows calculated natural frequency for such rectangular plate with two clamped edges. Only first natural frequency has been calculated. It can be seen that the natural frequency is dependent on plate dimensions. Also, different curves represent different values of flexular rigidity.

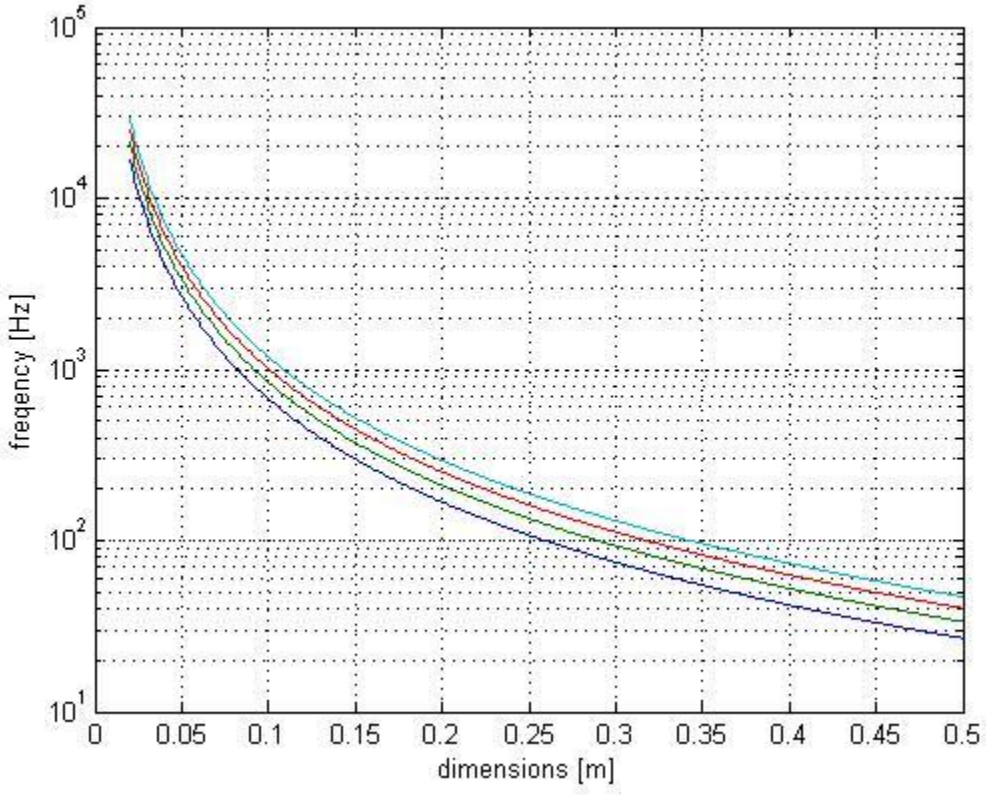

Figure 28. First eigenfrequencies for a rectangular plate with two clamped and two free edges

As it can be seen from the figure, several parameters influence the plate's eigenfrequencies. The first and the most obvious factor are the plate dimensions. The other factor is flexular rigidity of the plate. Greater the flexular rigidity, greater the resonant frequency of the plate. The flexular rigidity of the plate can be increased in several ways.

One option is to use the material with greater Young's modulus. However, apart from the fact that this is not the most efficient way of increasing the flexular rigidity, the introduction of new materials requires changes or adaptations in the production process, which inevitably lead to the increase of the manufacturing costs. This leads to another option, which is increasing the thickness of the board. This is not only more cost effective, but also has greater impact on flexular rigidity.

4.1.1 Modal (Eigenvalue) analysis

In dynamic eigenvalue analysis, we find the solution to an undamped linear dynamics problem

$$[K - \omega^2 M]\phi = 0$$

Where K is the stiffness matrix, M is the mass matrix, ω are the eigenvalues ϕ and are the eigenvectors. In Marc, if the extraction is performed after increment zero, K is the tangent stiffness matrix, which can include material and geometrically nonlinear contributions. The mass matrix is formed from both distributed mass and point masses.

There are several numerical methods available in MSC.Marc. Here, Lanczos method had been used, which is the most efficient eigenvalue extraction algorithm (3).

The simulation has been conducted on a PCB with 2x2 array CSP (Chip Size Package). PCB has 40x40 mm dimensions with 1.6 mm thickness. CSP has 2x2 mm dimensions with 0.7 mm thickness and four solder joints with 300 μm diameter and 200 μm height.

The model consists of 61578 elements and 67107 nodes. Element type is HEX7 which is an eight-node, isoparametric, hexahedral (three-dimensional, eight node, first-order arbitrarily distorted brick). The element uses trilinear interpolation functions, so for more accurate representation of bending characteristics it is advised to use more elements, i.e. finer mesh. (3)

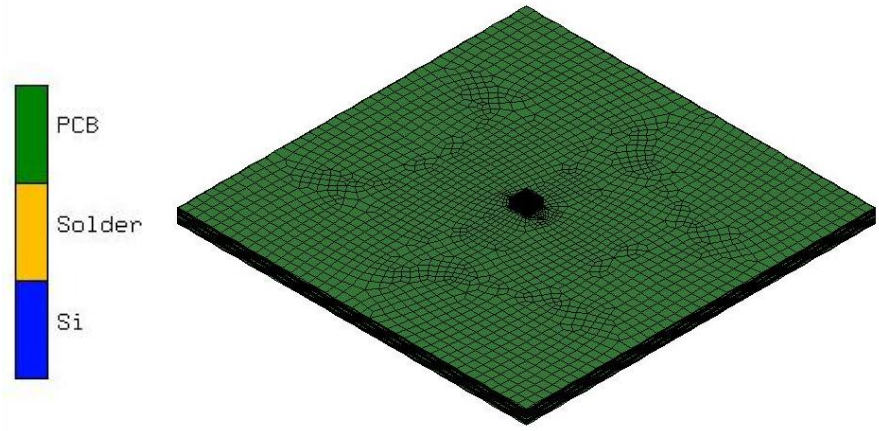

Figure 29. 3D view of FEM CSP soldered on a PCB

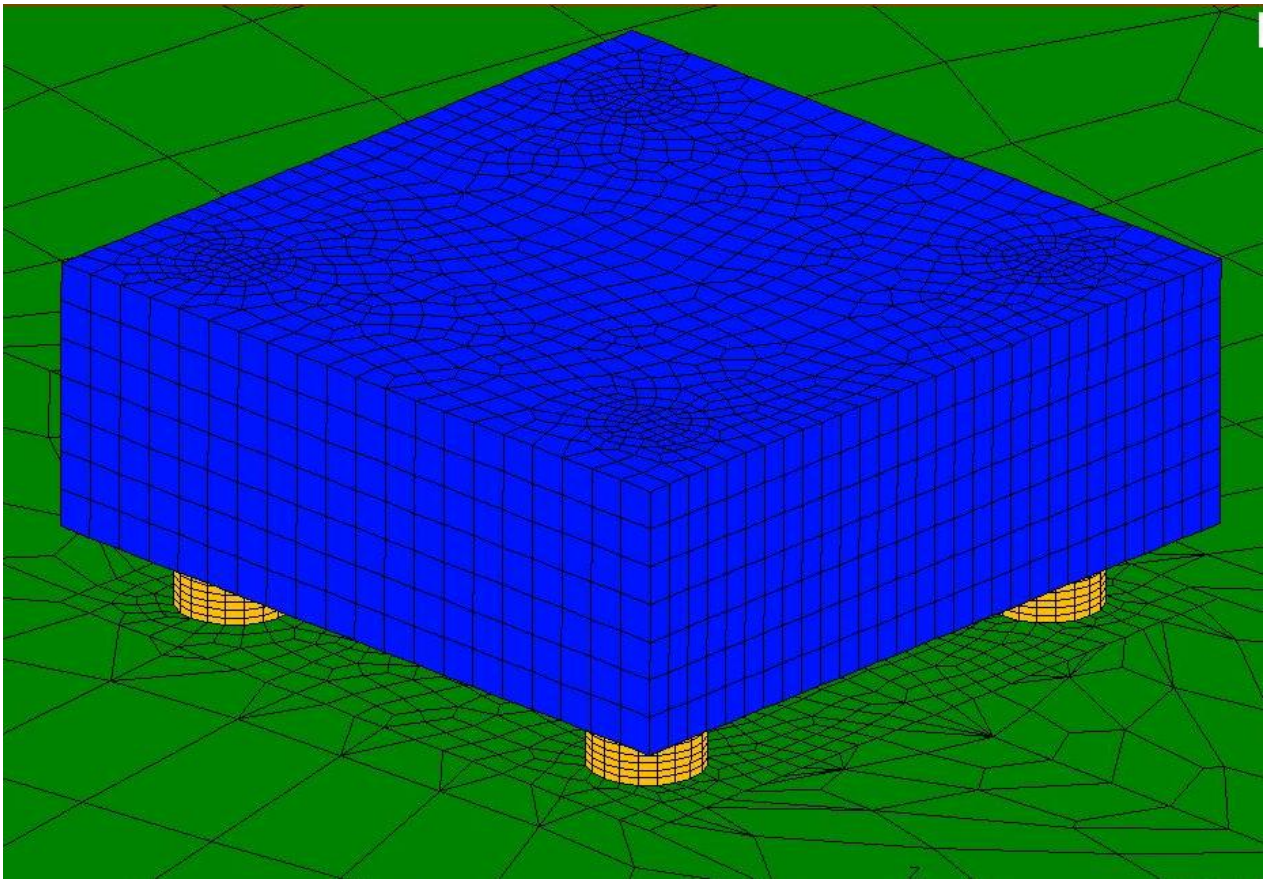

Figure 30.Detailed view of CSP with four solder joints

The material properties are given in the following table:

	Young's modulus [Mpa]	Poisson ratio	Mass density [Ns^2/mm^4]
PCB	25000	0.15	$1.5 \cdot 10^{-9}$
Solder	50000	0.4	$7.5 \cdot 10^{-9}$
CSP (Si)	169000	0.278	$2.33 \cdot 10^{-9}$

Several boundary conditions were tested, in order to determine their influence on dynamic behavior of the PCB.

These are:

- Two clamped edges, two free edges
- All four edges clamped
- Tightened with four screws
- Tightened with eight screws

The boundary conditions are depicted in the following figure

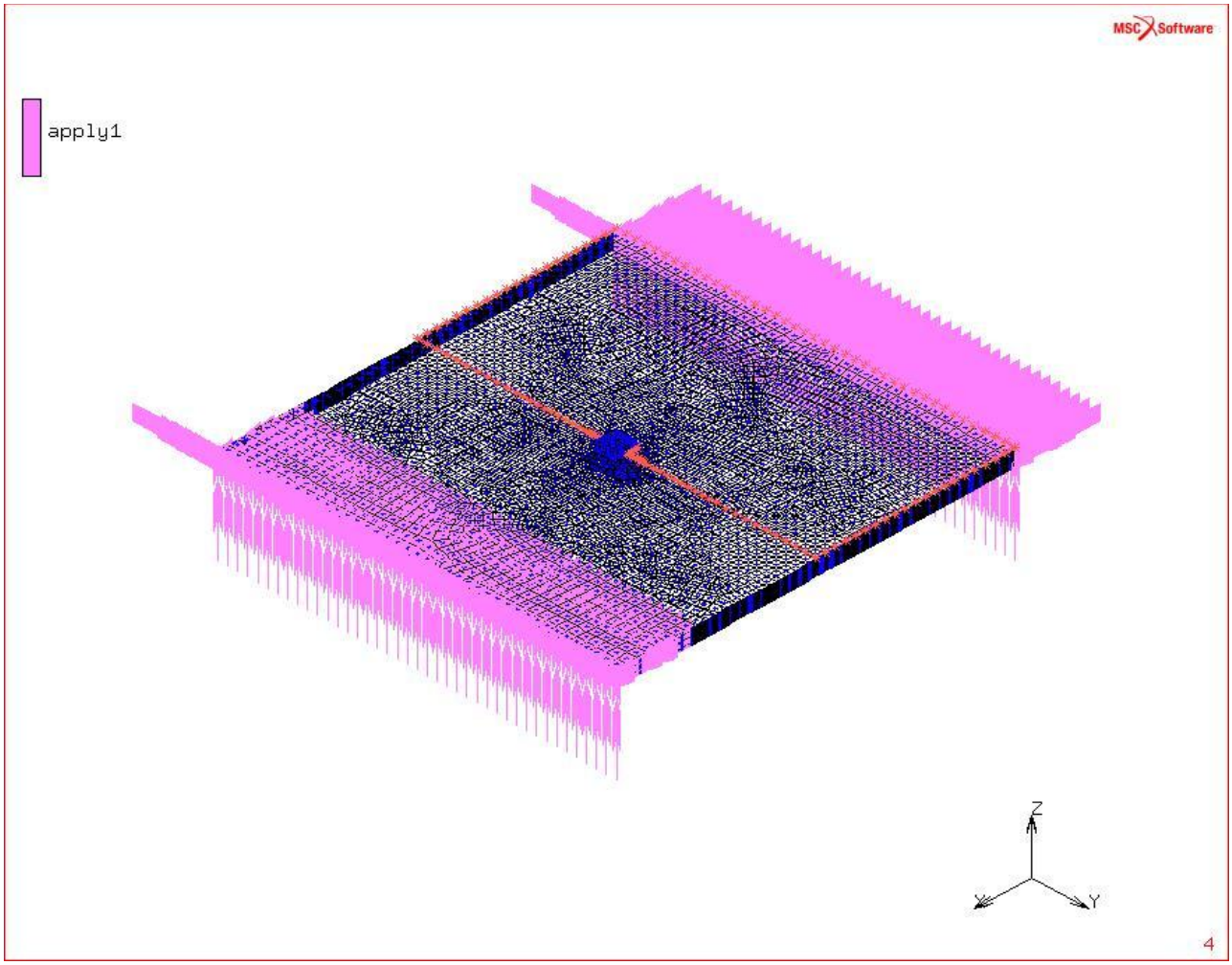

Figure 31. Boundary conditions – two edges clamped

As mentioned in 4.1.1chapter, Lanczos method has been used to determine first three modes of vibration and their corresponding eigenfrequencies.

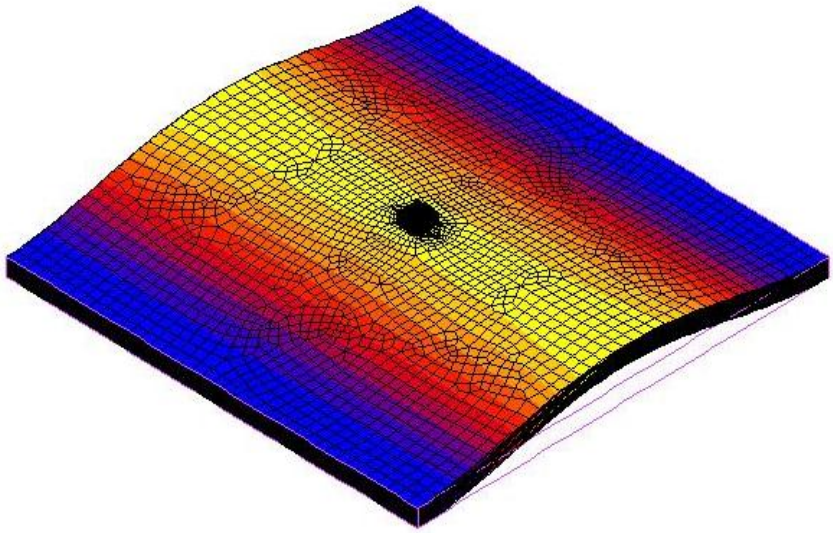

Figure 32. First mode of a PCB with two edges clamped

The corresponding eigenfrequency for the first mode is $f_n = 4197\ Hz$.

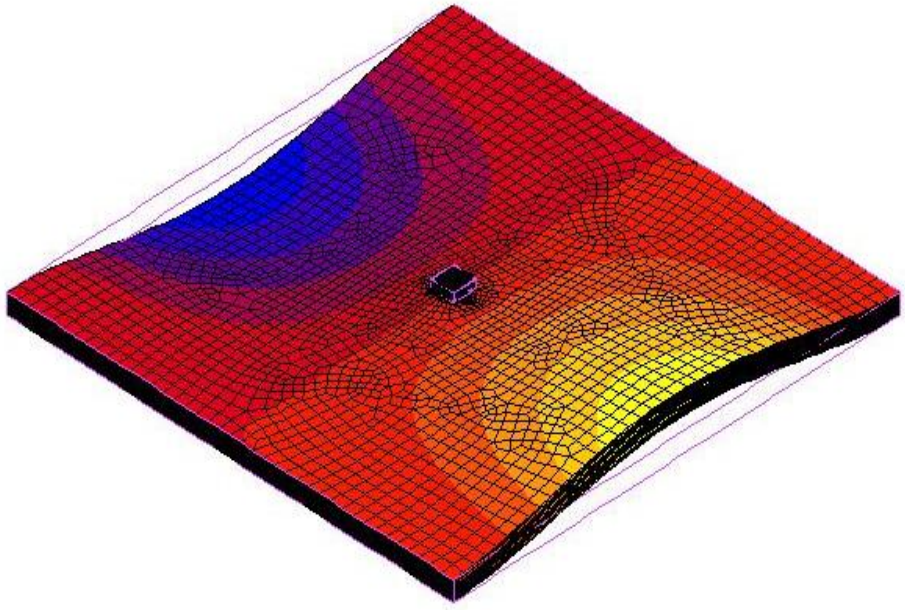

Figure 33. Second mode of a PCB with two edges clamped

The corresponding eigenfrequency for the second mode is $f_n = 5093\ Hz$.

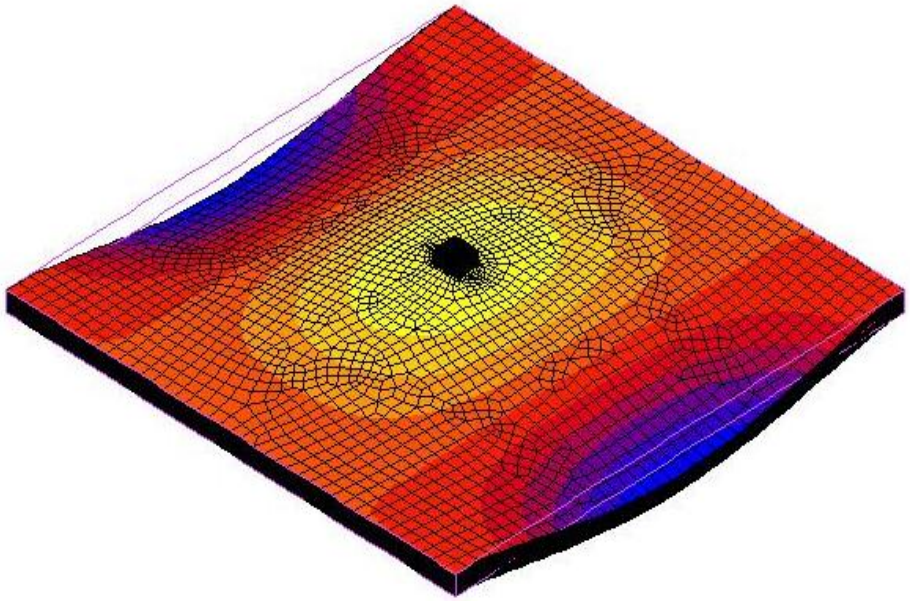

Figure 34. Third mode of a PCB with two edges clamped

The corresponding eigenfrequency for the third mode is $f_n = 8300\ Hz$.

There are several reasons for such high frequencies. First and most important ones are the dimensions of the PCB. As it can be seen from the Fig. 15, smaller the dimensions, greater the natural frequencies. The figure contains frequencies only for the first mode, but the same principle is holds value for all other modes.

The other reasons are the boundary conditions. The more the PCB is "confined", higher the resonant frequencies. This can be seen from the next example, where the PCB has all four edges clamped. However, this not only changes the resonant frequencies, but also the mode shapes. This can be seen from the following figures.

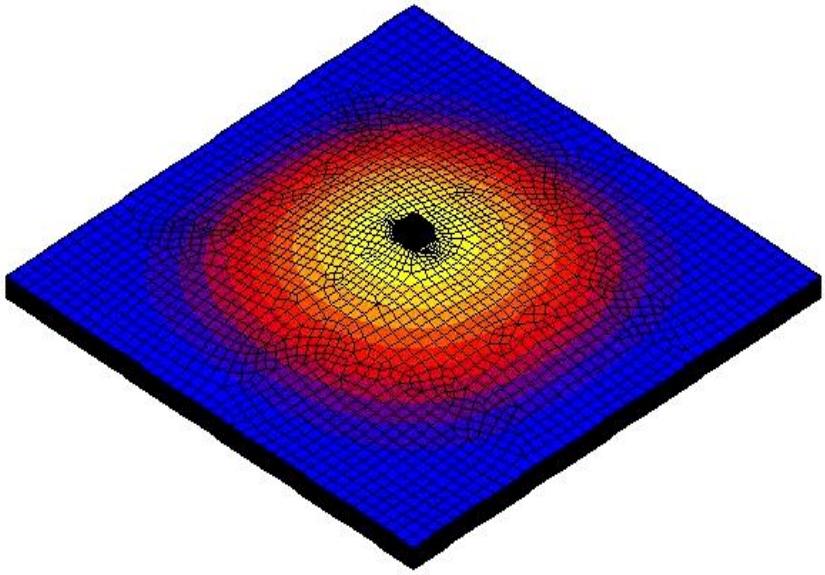

Figure 35. First mode of a PCB with four edges clamped

The corresponding eigenfrequency for the first mode is $f_n = 6707\ Hz$.

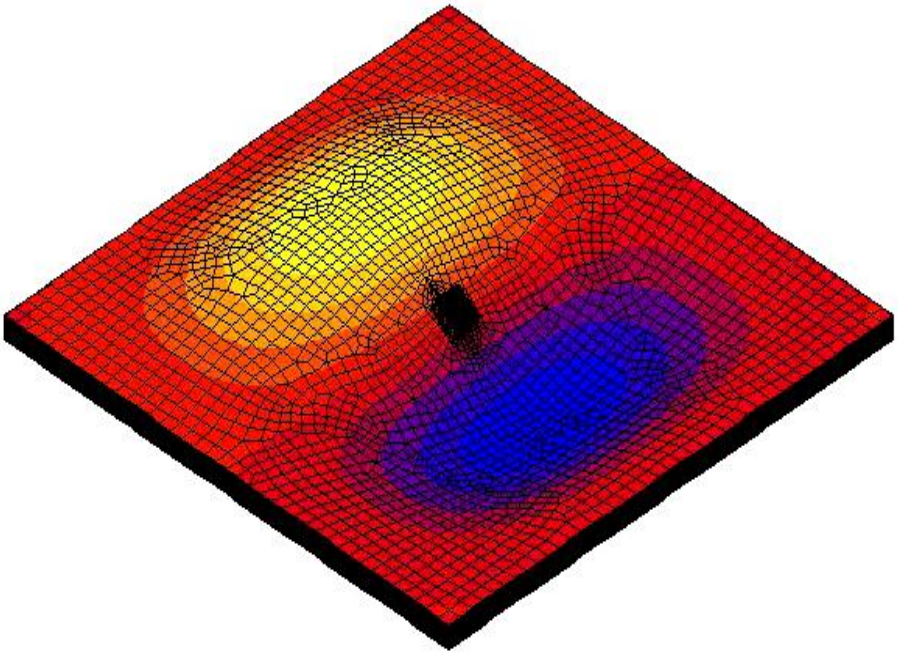

Figure 36. Second mode of a PCB with four edges clamped

The corresponding eigenfrequency for the second mode is $f_n = 13610\ Hz$.

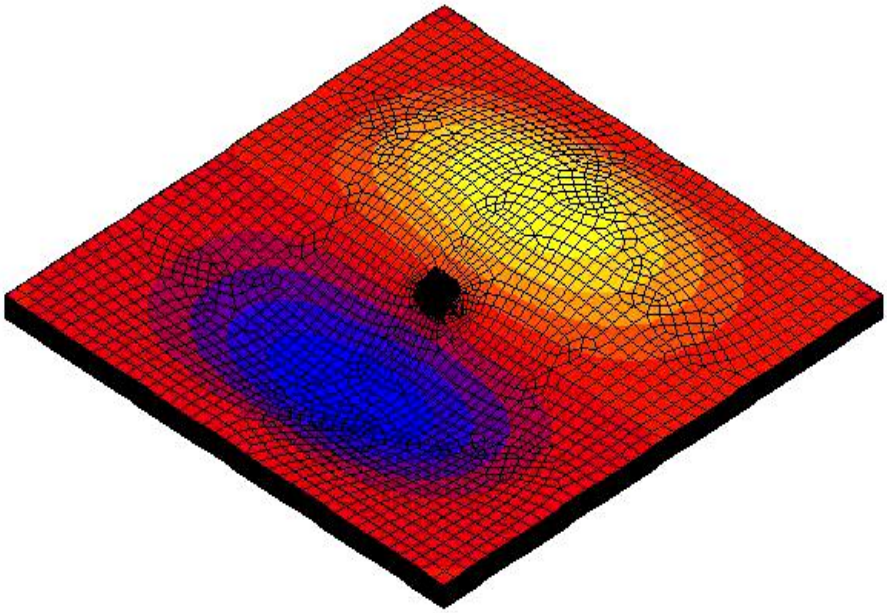

Figure 37. Third mode of a PCB with four edges clamped

The corresponding eigenfrequency for the third mode is $f_n = 13610\ Hz$.

Apart from higher eigenfrequencies and different mode shapes, another conclusion can be drawn from this example.

We can see that second and third mode have exactly the same eigenfrequencies at $f_n = 13610\ Hz$ and same mode shapes (rotated by 90 degrees).

The reason for this can be seen in the equation for simply supported plate. As m and n parameters are changed, the mode shapes remain the same but rotate, and the eigenfrequencies remain the same.

For instance, in the first case *m*=1, *n*=2, and in the second *m*=2, *n*=1. Substituting these values in the equation for the simply supported plate and keeping other values same (as the same plate is being analyzed) we will get the same eingenfrequencies and same mode shapes. This is true not only for the simply supported plate, but also for some plates with different boundary conditions, in this case a PCB with all four edges clamped.

The next PCB to be analyzed is a PCB tightened with four screws. The boundary conditions are depicted in the following figure

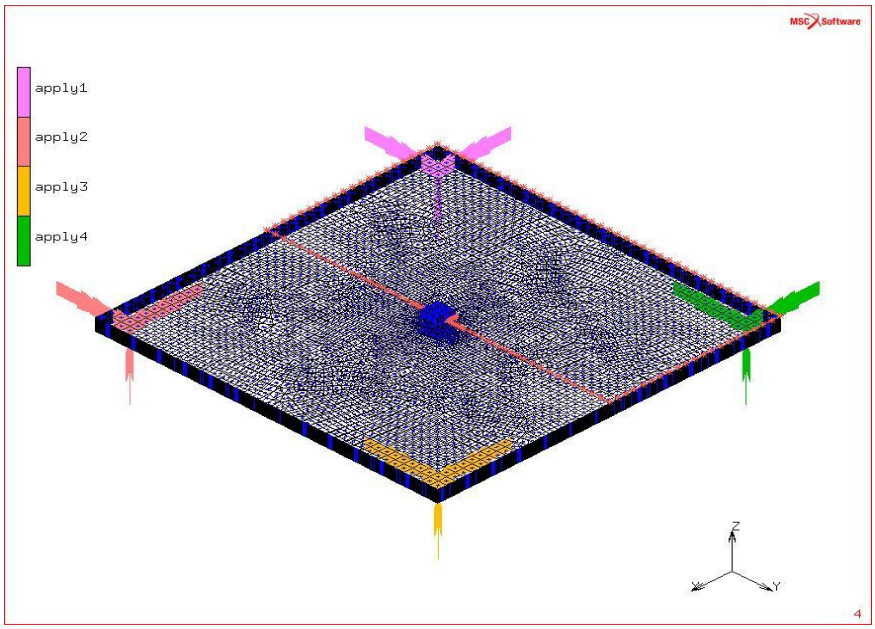

Figure 38. Boundary conditions for a tightened PCB with four screws

Modal analysis gave the following results

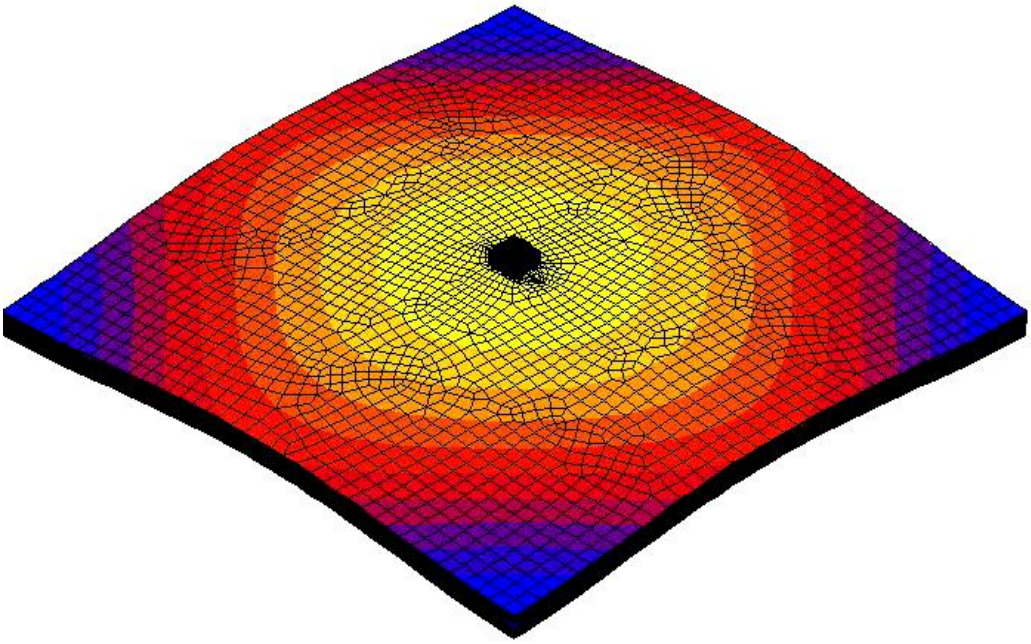

Figure 39. First mode of a tightened PCB with four screws

The corresponding eigenfrequency for the first mode is $f_n = 2427\ Hz$.

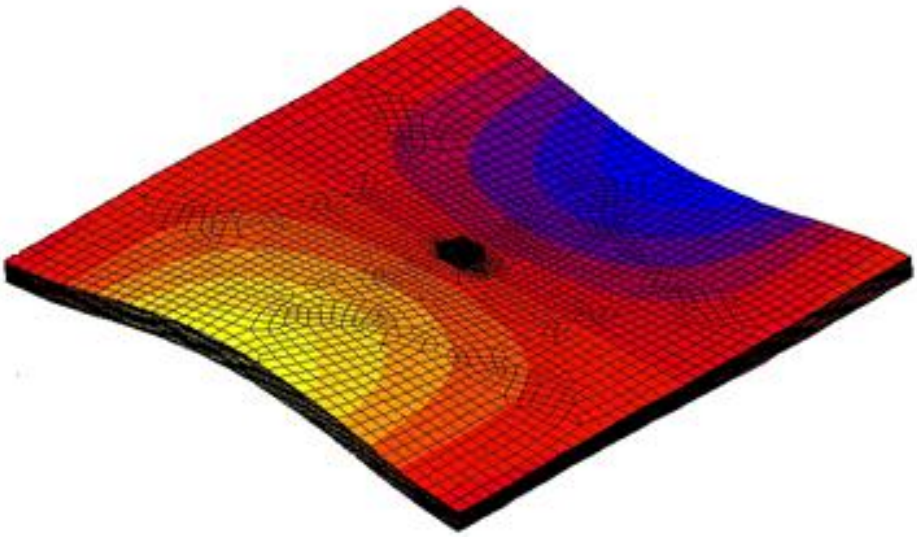

Figure 40. Second mode of a tightened PCB with four screws

The corresponding eigenfrequency for the second mode is $f_n = 4723\ Hz$.

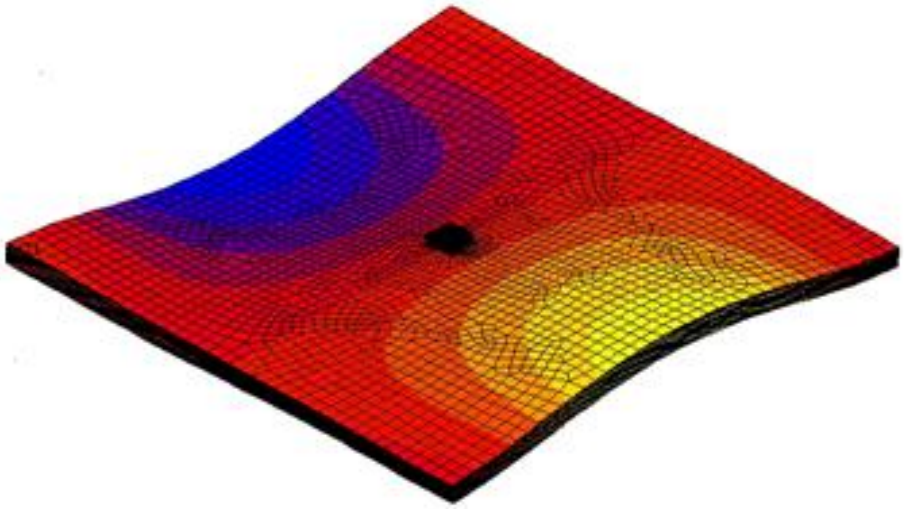

Figure 41. Third mode of a tightened PCB with four screws

The corresponding eigenfrequency for the third mode is $f_n = 4723\ Hz$.

As it can be seen, in this example, the eigenfrequencies are significantly lower than in previous two cases. This can be contributed to the different boundary conditions or less "constraining" boundary conditions.

Also as in the previous example, second and third eigenmodes have identical eigenfrequencies.

In this example the PCB was tightened with eight screws.

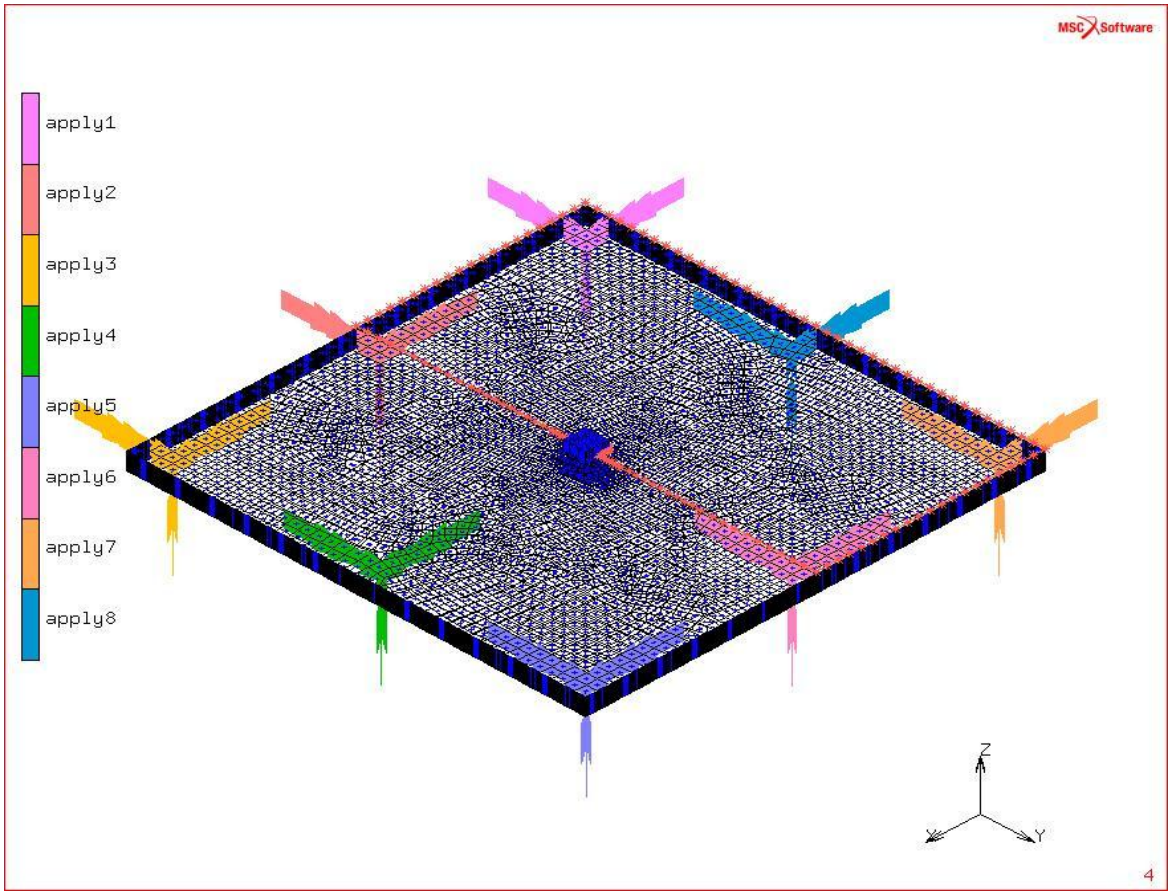

Figure 42. Boundary conditions for a tightened PCB with eight screws

Modal analysis gave the following results:

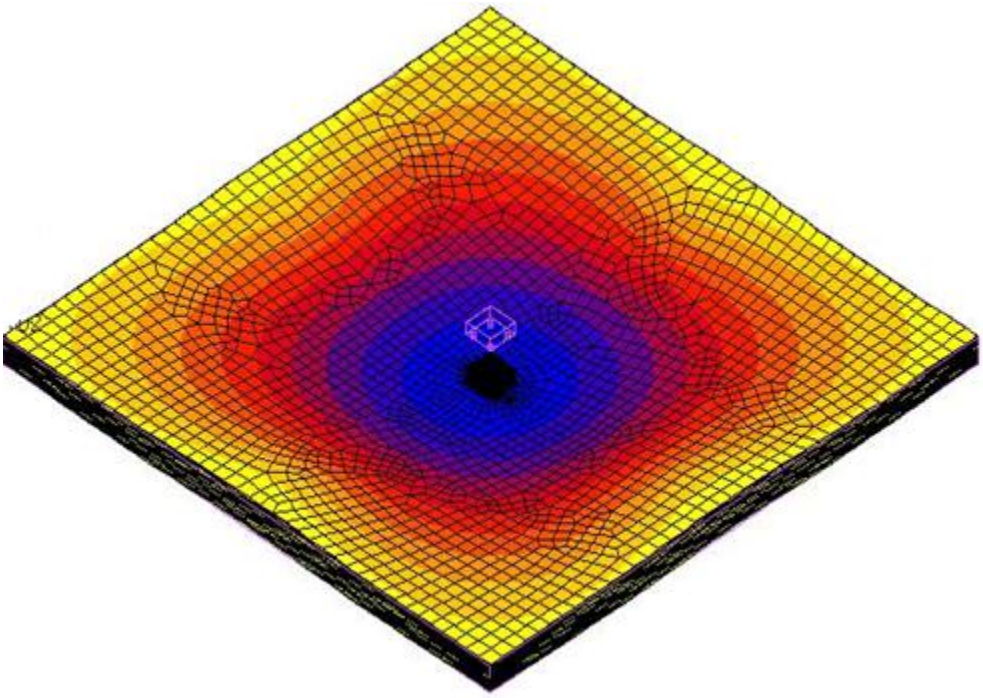

Figure 43. First mode of a tightened PCB with eight screws

The corresponding eigenfrequency for the first mode is $f_n = 5577\ Hz$.

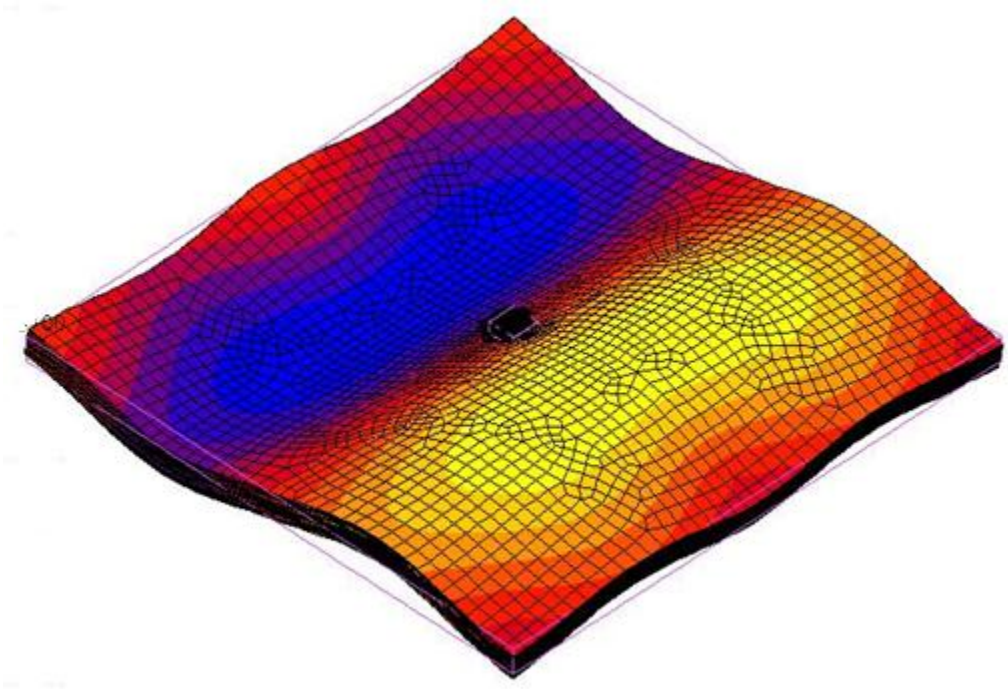

Figure 44. Second mode of a tightened PCB with eight screws

The corresponding eigenfrequency for the second mode is $f_n = 10250\ Hz$.

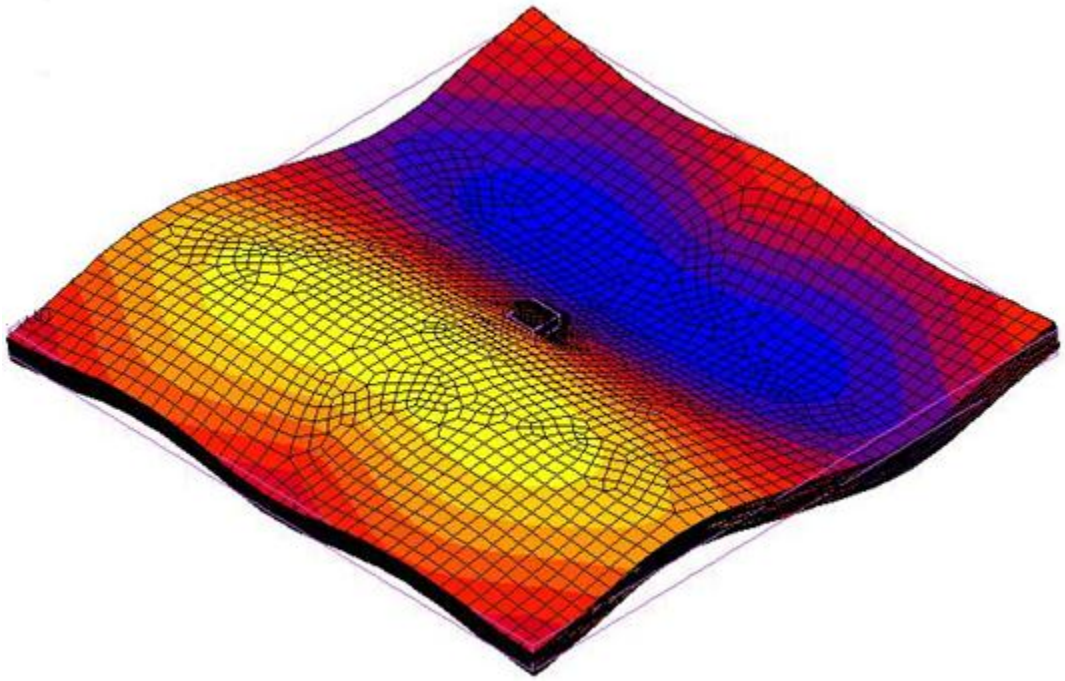

Figure 45. Third mode of a tightened PCB with eight screws

The corresponding eigenfrequency for the third mode is $f_n = 10330\ Hz$.

The same trend as in previous examples can also be seen here. Eigenfrequency is increased and mode shapes are different. In many ways this example is similar to fully clamped PCB in both eigenfrequency values and mode shapes.

Few general conclusions can be drawn from this analysis. For same boundary conditions, the dimensions increase will lead to lower eigenfrequencies. Increasing flexular rigidity will in turn increase the eigenfreguencies. This can be seen from Figure 28. First eigenfrequencies for a rectangular plate with two clamped and two free edges .

For same dimensions changing the boundary conditions will cause changes both in eigenfrequencies and mode shapes. Less constraining boundary conditions will significantly lower the eigenfrequencies. This means that in the case of pure vibration loading, more constrained PCBs will have higher fatigue life than less constrained PCBs.

4.2 Thermal fatigue analysis

In this section the focus will be on PCB under pure thermal cycling.

As mentioned in the introduction thermal cycling conditions (-40 to +125 degrees Celsius) are selected based on JEDEC temperature cycling standard (JESD22-A104-B). This temperature range suffices to investigate typical product cycle within -40 to +90 degrees Celsius, which is usually seen in for the avionics components. The character of thermal cycling is seen in the following figure. The PCB layout remained the same.

It is important to mention that this is not the analysis of heat transfer within the material. It is assumed that at each temperature level, all elements are at that specific temperature level.

As plasticity is time independent material property, time has no effect on accumulation on plastic strain.

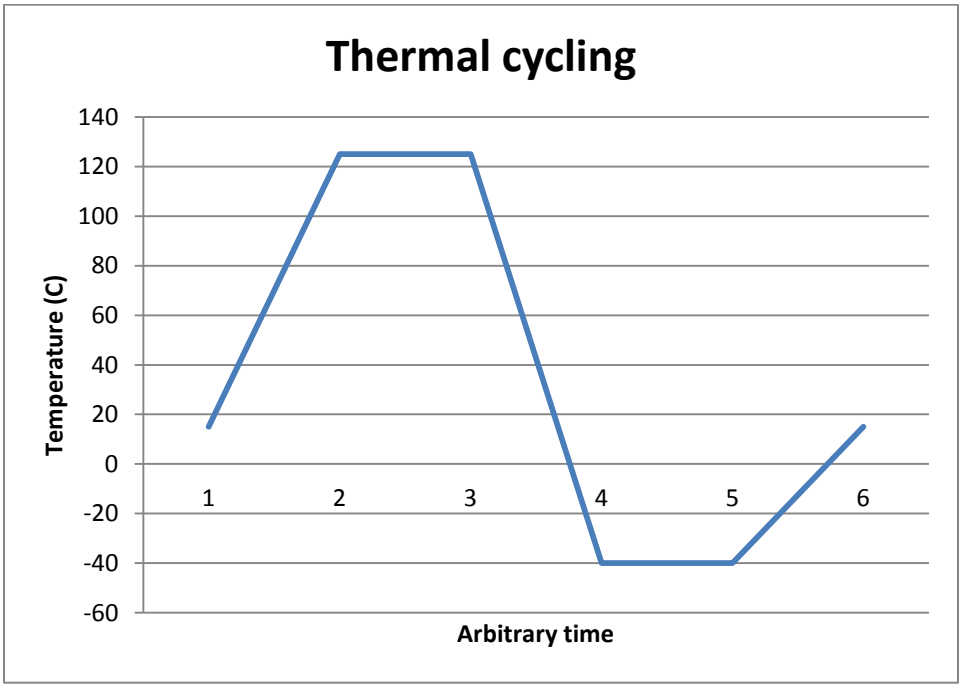

Figure 46. Thermal cycling

The material properties are given in the following table:

	Young's modulus [MPa]	Poisson ratio	Mass density [Ns^2/mm^4]	Coefficient of thermal expansion (CTE)
PCB	25000	0.15	$1.5 \cdot 10^{-9}$	$1.5 \cdot 10^{-5}$
Solder	50000	0.4	$7.5 \cdot 10^{-9}$	$1.8 \cdot 10^{-5}$
CSP (Si)	169000	0.278	$2.33 \cdot 10^{-9}$	$1.8 \cdot 10^{-5}$

The solder behaves like elastic-perfectly plastic material with the yield strength of the solder is 25.68 MPa. The PCB and CSP behave like ideal elastic materials.

The PCB has two edges clamped. Also, the entire PCB (and its components) is continuously heated and cooled as shown in the previous figure.

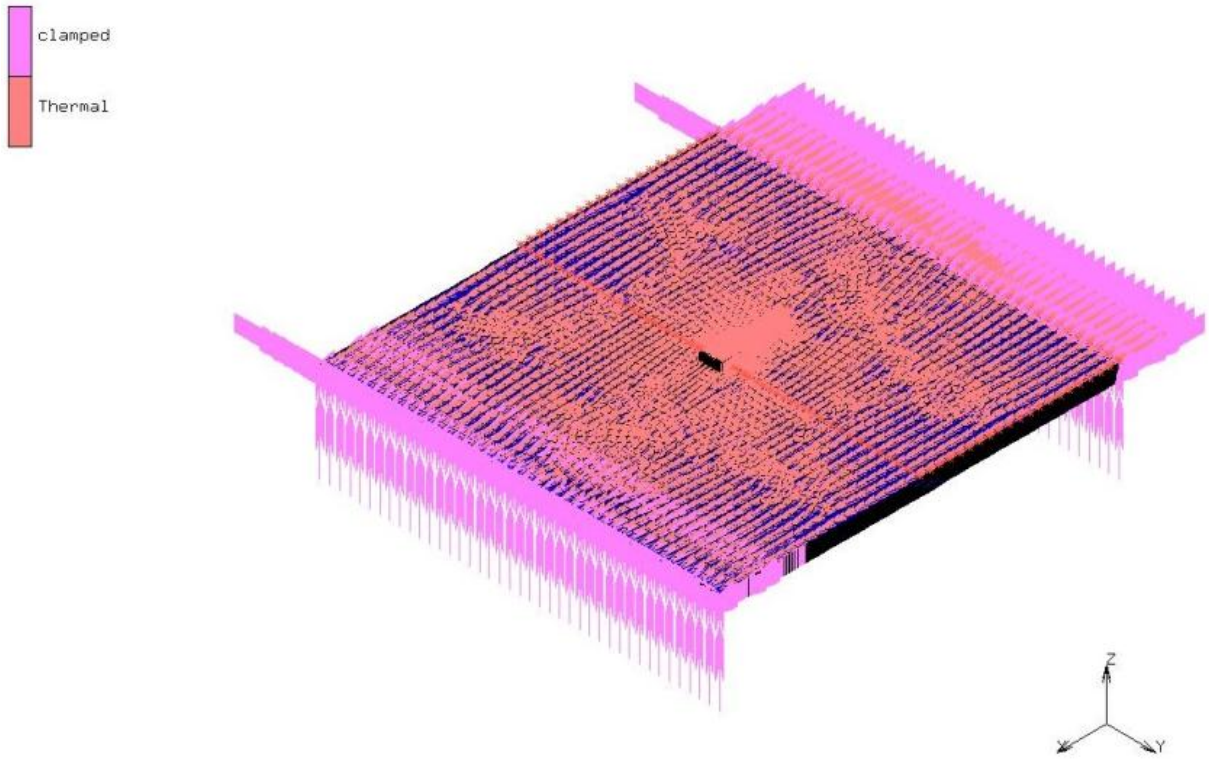

Figure 47. Boundary conditions for pure thermal cycling

The main goal during this analysis is to determine the plastic behavior of solder. This is determined by calculating the plastic strain within the solder. Plastic strain is then used in fatigue models to determine the life of solder.

For PCB with two edges clamped, thermal analysis gave following results.

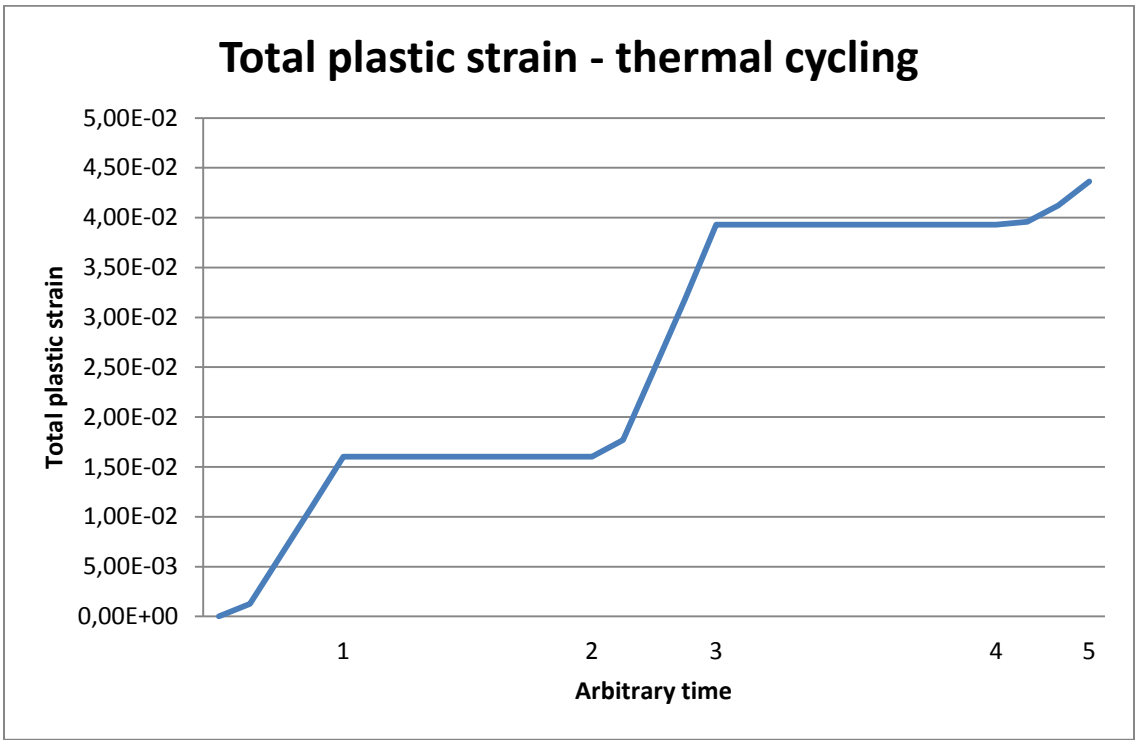

Figure 48. Total equivalent plastic strain for thermal cycling

As it can be seen, plastic strain is accumulated during both heating and cooling process. Also, during dwell period (periods of constant temperature, -40 and +125 degrees Celsius) there is no accumulation of plastic strain within the solder. This is expected as plasticity is time independent behavior (unlike creep).

The total plastic strain range of one cycle is $\Delta\varepsilon_{pl,TC} = 4.36\%$. This information is later used in fatigue models to determine the number of cycles to failure.

The critical part of the solder is the area of connection with the PCB. These are the areas of the highest plastic deformations and areas where the crack is likely to occur. This is caused by the mismatch between coefficients of thermal expansion between the solders and the PCB. The solder behavior is dominated by shear deformation.

The areas of highest plastic deformations can be seen in the following figure. In this case, the outside connection area with the PCB is the critical one.

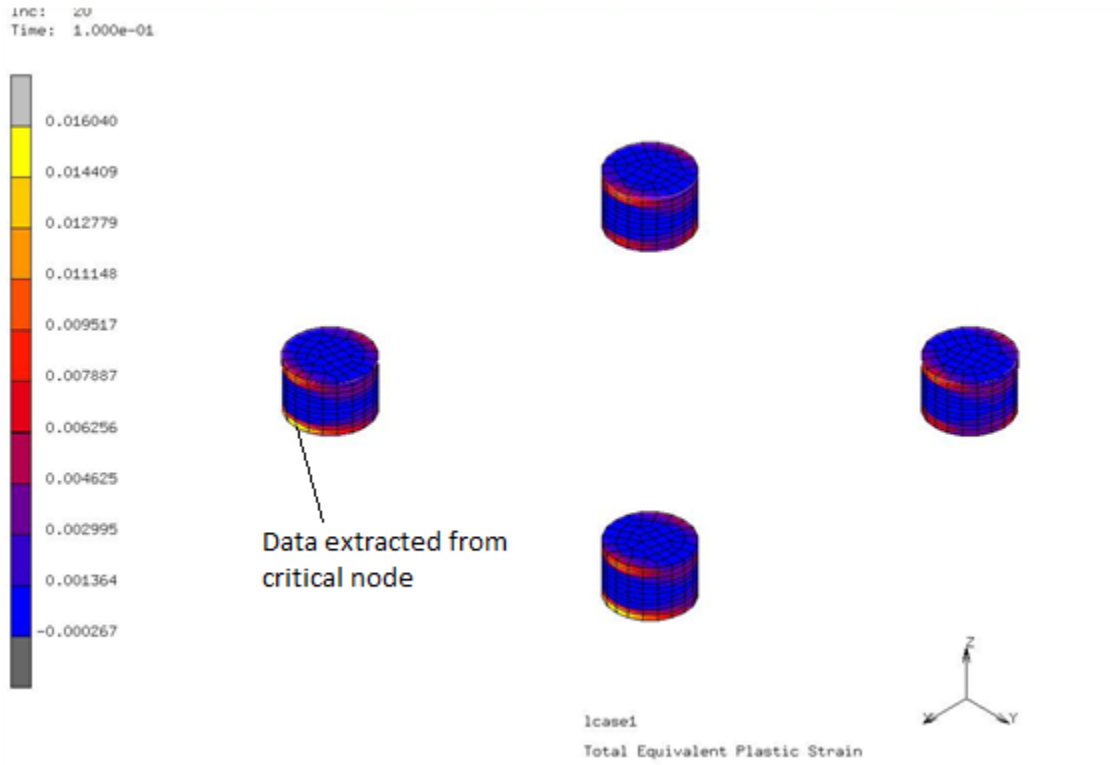

Figure 49. Plastic strain in solders – thermal cycling

4.3 Combined loading fatigue

The final step is to conduct the analysis of combined loading. It is assumed that during thermal cycling, the periods of constant temperature are usually significantly longer than ramp periods (periods of heating up and cooling down), so additional vibration loading is modeled only during periods of constant temperature. In these two periods, the previously clamped edges of the PCB start moving in the direction of the *z* axis. In this way it is easier to assess the damage from additional vibration loading. Also, the vibration loading is modeled as triangle shape loading, due to the practical reasons and technical limitations.

The profile of vibration loading can be seen in the following figure

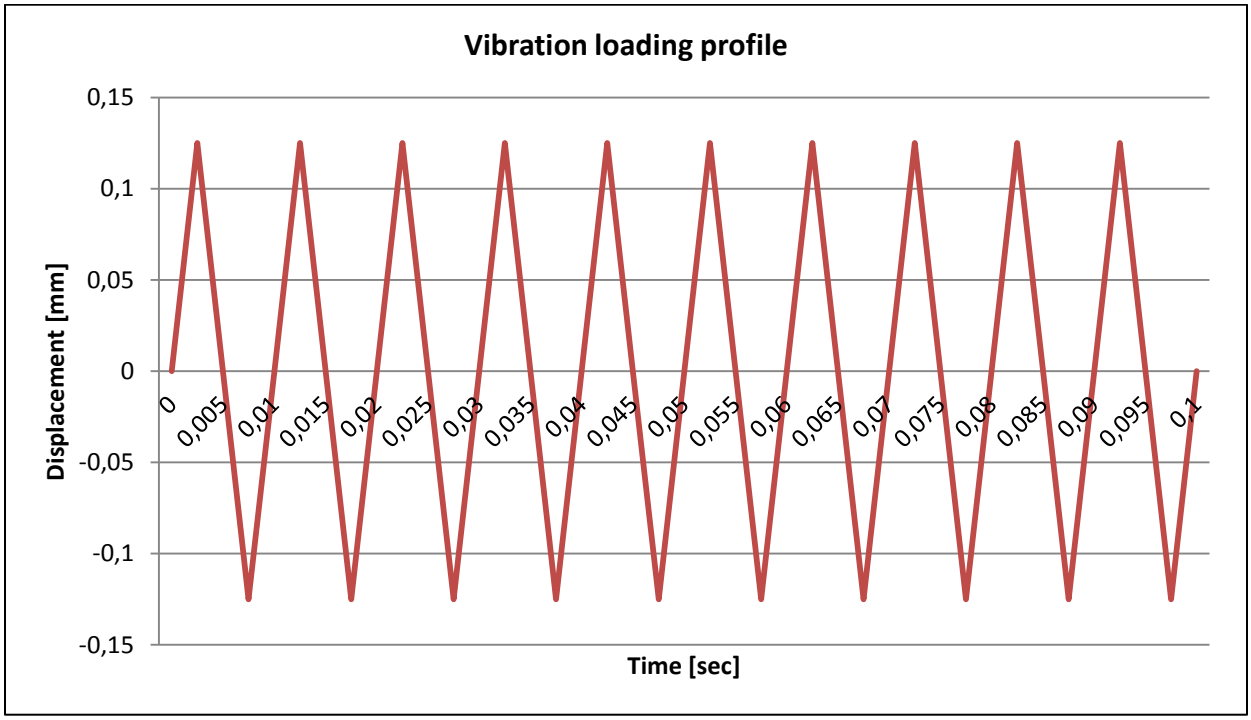

Figure 50. Vibration loading profile

The amplitude of the loading is 0.125 mm which is approximately equivalent to 5G and can be found in most aircraft. Also, the frequency of the loading is 100 Hz, which is also typical for most aircraft. For this simulation the total of 10 vibration cycles have been used. This was due to the technical limitations, as modeling a big number of cycles will lead to extremely long analysis time. Due to the low $R_\Omega = 0.024$, it is not necessary to include damping in the model, as it will have no effect on the displacement of the PCB.

The vibrations will cause a maximum displacement in the middle of the PCB of 0.125078 mm.

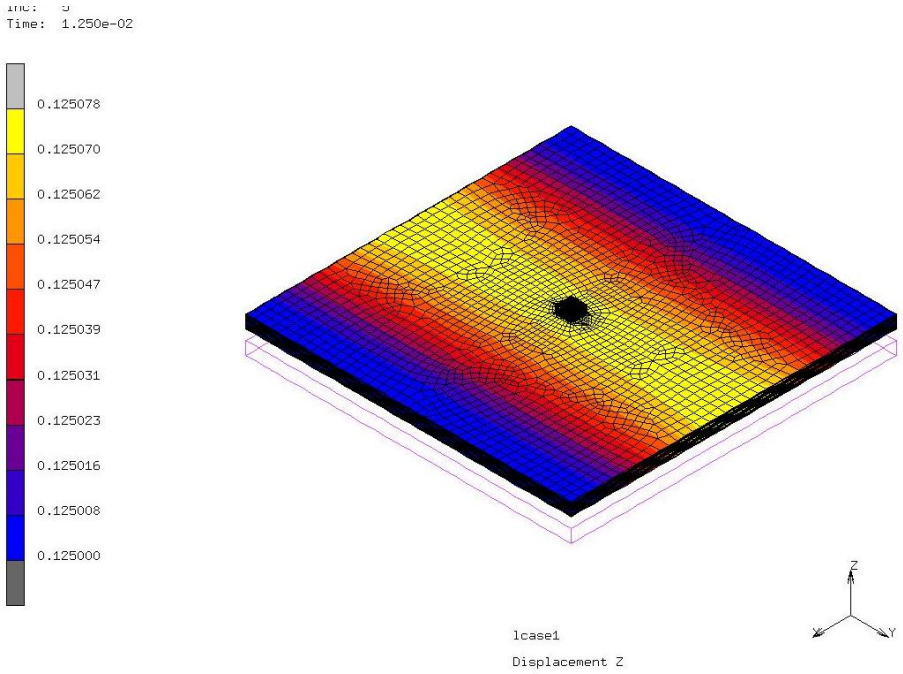

Figure 51. Displacement of the PCB

The profile of the combined loading is seen in the following figure.

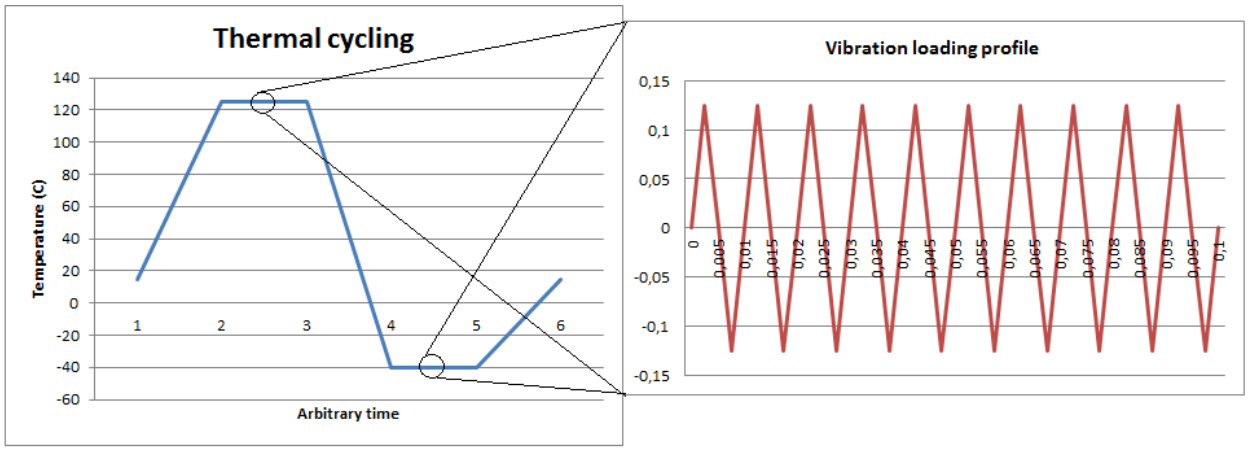

Figure 52. Profile of combined loading

The influence of vibration can be assessed comparing end points (times) of periods of constant temperature. For pure thermal cycling these points (for instance points 2 and 3) have the same value (same total plastic strain). However, with combined loading point 3 will have greater value than point 2 (total plastic strain is greater in point 3 than point 2). This can be used to calculate vibration induced total plastic strain.

At the beginning of the first period of constant temperature (125 degrees Celsius temperature period), the total plastic strain is equal as in the case of pure thermal loading. However, due to the additional vibration loading an increase in total plastic strain can be seen at the end of the period.

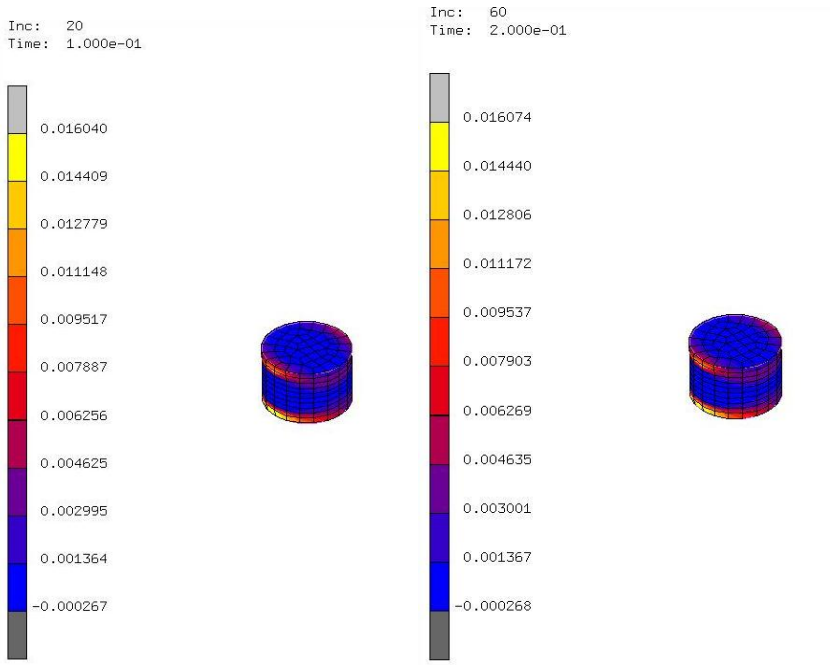

Figure 53. Comparison of total plastic strain in solders at the end points of the constant temperature period

Knowing the difference in total plastic strain at two end points and the number of cycles it is possible to determine induced total plastic strain for one vibration cycle.

In this case, the calculated induced total plastic strain for one vibration cycle is

$$\Delta\varepsilon_{pl,vib} = 0.000218\%$$

Such low value (significantly lower than thermally induced plastic strain) was expected. As in the case of pure thermal cycling, this information can be used in fatigue models to determine time to failure of the component.

However, due to take lack of data on material properties at such extreme temperatures and frequency loading, only general assumptions can be made.

Here a fatigue developed by (11) had been used. It must be noted that this is a low cycle fatigue model which had been extrapolated to assess the vibration induced damage. This will not give completely accurate results, but will show the influence of each type of loading on time to failure.

In this fatigue model, number of cycles to failure is equal to

$$N_f = 1427 \cdot (\Delta\varepsilon_{pl})^{-1.433}$$

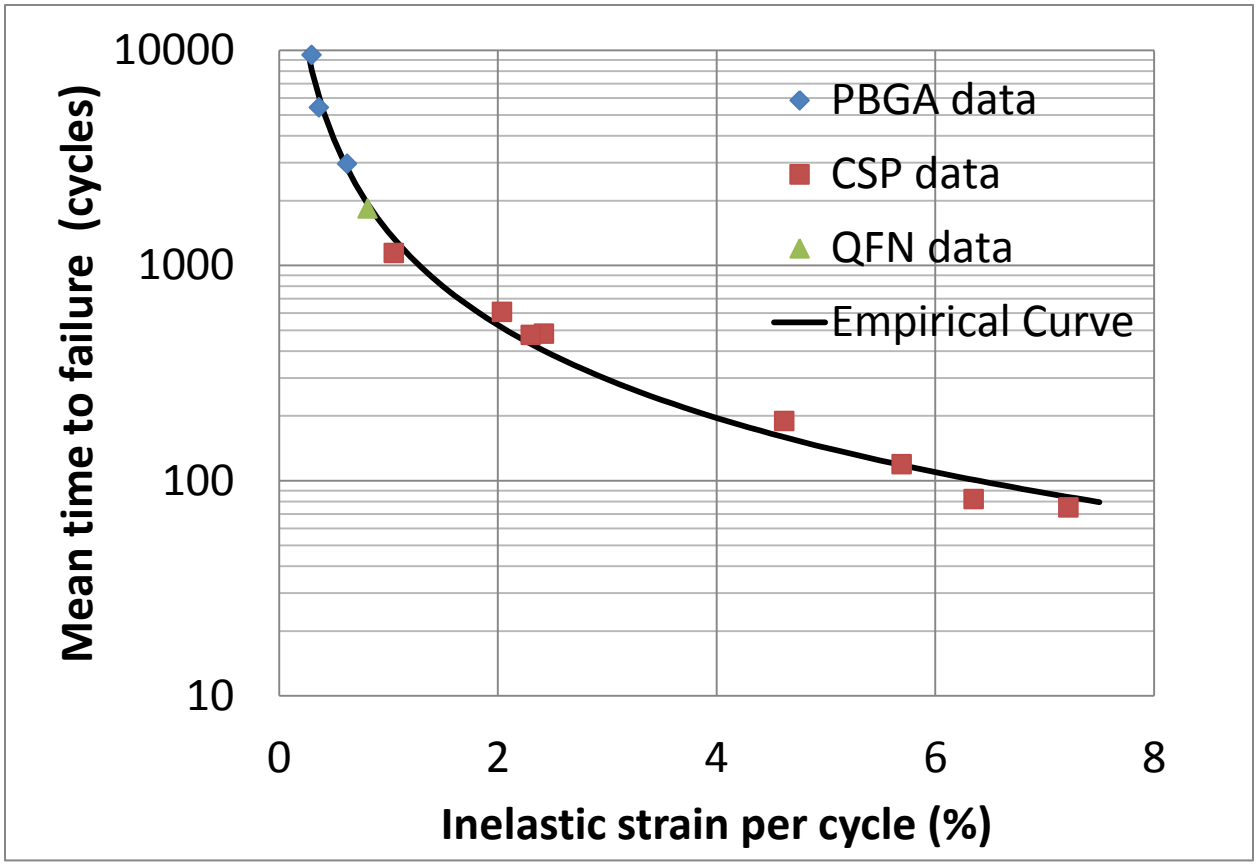

Figure 54. Used fatigue model (11)

Where the $\Delta\varepsilon_{pl}$ is entered in percentage.

For pure thermal cycling loading (one thermal cycle), number of cycles to failure, damage and time to failure can be calculated as

$$N_{f,TC} = 1427 \cdot (4.36)^{-1.433} \cong 173\ cycles$$

Damage in one cycle is

$$D_{TC} = \frac{1}{N_{f,TC}} = 0.00578$$

For one hour thermal cycling time to failure is

$$TTF_{TC} = \frac{1}{D_{TC}} \cong 173\ hours$$

The empirical model is used to assess the vibration number of cycles to failure, damage and time to failure. This just a zero-order estimation as the empirical model is extrapolated to very low strain values. It is assumed that vibrations are present for one hour in each thermal cycle.

$$N_{f,Vib} = 1427 \cdot (0.000218)^{-1.433} \cong 2.5 \cdot 10^{8}\ cycles$$

Damage in one cycle is

$$D_{Vib} = \frac{1}{N_{f,Vib}} = 3.968 \cdot 10^{-9}$$

Damage in one hour is

$$D_{Vib} = 0.001429$$

Time to failure is

$$TTF_{Vib} = \frac{1}{D_{Vib}} \cong 700\ hours$$

Now the damage from 1 hour thermal cycling and vibration loading can be added to calculate the time to failure for combined loading.

$$D_{total} = D_{TC} + D_{Vib} = 0.007209$$

And the total time to failure is

$$TTF_{total} = \frac{1}{D_{total}} \cong 139\ hours$$

As it can be seen, additional vibration loading will cause the failure more than 40 hours sooner, than in the case of pure thermal cycling. For pure vibration loading, time to failure is much longer, approx. 700 hours. This is also expected as vibrations alone are not the primary cause of failures in electronic equipment. But as can be seen, they will accelerate time to failure.

However, to accurately assess the damage for combined loading it is necessary to conduct experiments to develop the more accurate fatigue model for combine loading conditions.

5 Conclusion

The goal in this thesis was to develop the FEM based methodology for combined thermal and vibration loading, which can be used in determining the fatigue life of electronic equipment under such loading.

This was not an easy task, as there were several obstacles; lack of data on solder behavior under such type of loading, which means the results cannot be experimentally validated, Moreover CPU limitations do not allow to preform detailed vibration and thermal cycling loading and this, impose simplifications in modeling in order to obtain the results in the reasonable amount of time.

However, even with all these limitations, the developed method showed promising results. For period of constant temperature, it is possible to assess the vibration induced damage. It is also not necessary to use the actual number of cycles for the analysis. This leads to significantly lower analysis time. The method also gave the results that were within the expectations regarding the fatigue life.

The analysis showed that thermal loading is the primary cause of failure. This can be seen when comparing the time to failure between the pure thermal and pure vibration loadings. However, adding the vibration to thermal loading will have significant impact on fatigue life of electronic equipment. This impact will have an even greater effect when the frequency of the vibration loading is increased. It is therefore necessary to take vibrations into the account if the correct fatigue life has to be determined.

However it must be taking into the account that the fatigue model used here is not completely suited for assessing the vibration induced damage, which means that the actual time to failure will actually be different from the one calculated. In order to have full confidence into the results it is necessary to conduct required experiments, which will lead to developing an accurate fatigue model for combined loading. Another improvement is the inclusion of random vibrations. Here, the vibrations have triangular signal as a replacement for sine signal, but in real world applications vibrations are mostly random in nature.

This will set the basis for future work, which should lead to creating accurate fatigue model for determining the fatigue life of electronic equipment under combine loading.

6 Works Cited

1. **Moir, Ian and Seabridge, Allan.** *Aircraft Systems - Mechanical, electrical, and avionics subsystem integration.* Chichester : John Wiley & Sons, 2008.

2. *Plastic Ball Grid Array Solder Joint Reliability for Avionics Application.* **Qi, Haiyu, Osterman, Michael and Pecht, Michael.** 2, s.l. : IEEE Transactions on components and packaging technologies, 2007, Vol. 30.

3. *MSC.Marc 2010 Volume A: Theory and User Information.* 2010.

4. **Steinberg, Dave.** *Vibration Analysis for Electronic Equipment.* s.l. : John Wiley & Sons, 2000.

5. **Vandevelde, Bart.** *Reliability impact assessment of Green Mold Compounds.* 2011.

6. *Low Cycle Fatigue Prediction Model for Pb-Free Solder 96.5Sn-3.5Ag.* **Kanchanomai, C. and Muoth, Y.** 4, s.l. : Journal of Electronic Materials, 2004, Vol. 33.

7. *Investigation of the Solder Joint Fatigue Life In Combined Vibration and Thermal Cycling .* **Eckert, Tilman, et al., et al.** s.l. : IEEE, 2010.

8. **Timoshenko, S. and Woinowsky-Krieger, S.** *Theory of plates and shells.* s.l. : McGraw-Hill, 1959.

9. **Chakraverty, Snehashish.** *Vibration of Plates.* Boca Raton : CRC Press, 2009.

10. **Leissa, Arthur W.** *Vibration of plates.* s.l. : National Aeronautics and Space Administration, 1969.

11. **Vandevelde, Bart.** *Internal data - imec.*